Mechanistic insights into CFTR function from molecular dynamics analysis of electrostatic interactions

Ahmad Elbahnsi[1,2,*], Jean-Paul Mornon[1] and Isabelle Callebaut[1,*]

1 Sorbonne Université, Muséum National d'Histoire Naturelle, UMR CNRS 7590, Institut de Minéralogie, de Physique des Matériaux et de Cosmochimie, IMPMC, 75005 Paris, France
2 Université Paris Cité, CNRS UMR 8038 CiTCoM, Inserm U1268 MCTR, Paris, France

*co-corresponding authors: ahmad.elbahnsi@inserm.fr, isabelle.callebaut@sorbonne-universite.fr

Abstract

The Cystic Fibrosis Transmembrane Conductance Regulator (CFTR) is an ATP-gated anion channel whose function is tightly linked to its conformational dynamics and is influenced by the composition of its membrane lipid environment. Despite high-resolution three-dimensional (3D) structures, the molecular determinants that stabilize specific CFTR conformations and enable ion conduction remain incompletely understood. Here, we performed all-atom molecular dynamics (MD) simulations of the human CFTR 3D structure in both the apo and VX-770–bound states, embedded in a heterogeneous lipid bilayer, in order to systematically analyze electrostatic interactions, linking amino acids to each other as well as to anions and membrane lipids.

We identified 558 electrostatic interactions between charged and polar amino acid side chains, which we systematically mapped across the CFTR 3D structure. They are organized into specific regions, with a subset showing high frequency and conservation across simulations, suggesting a structural role in stabilizing CFTR architecture. In contrast, more transient electrostatic interactions were detected in dynamic regions potentially linked to conformational transitions or other functional roles. Irregularities in transmembrane (TM) helices often incorporate amino acids involved in electrostatic interactions. Many basic and polar residues involved in electrostatic interactions also engaged in anion coordination, underscoring their contribution to ion conduction. In addition, some showed selective interactions with cholesterol and phosphatidylserine, revealing spatially organized lipid binding, particularly at the level of the lasso and in the vicinity of the VX-770 binding site, which may mark regions important for allosteric communication. VX-770 binding preserved the global architecture of the electrostatic interaction networks but induced subtle shifts, reinforcing specific salt bridges and enhancing anion contacts, especially around a portal displayed between TM10/TM12. This one is located opposite to the main TM4/TM6 portal, whose morphology and diameter is controlled by a fluctuating salt bridge. Regardless of whether VX-770 is present or not, two exit routes also emerged from these MD simulations. Altogether, our integrative analysis highlights how dynamic electrostatic networks, together with ion and lipid interactions support CFTR's structural plasticity and functional modulation, offering molecular insights into potentiation mechanisms and into the specific evolution of CFTR in the ABC transporter superfamily.

Keywords: Cystic fibrosis, CFTR dynamics, Salt bridges, Hydrogen bonds, Electrostatic interactions, Anion efflux, Lipid interaction, MD simulations.

Abbreviations: 3D: three-dimensional, CHL: cholesterol, CF: Cystic Fibrosis, CFTR: Cystic Fibrosis Transmembrane Conductance Regulator, cryo-EM: cryo-electron microscopy, HB: Hydrogen Bond, SB: Salt Bridge, ECL: ExtraCellular Loop, TMD: TransMembrane Domain, ICL: IntraCellular Loop, TM: TransMembrane, NBD: Nucleotide Binding Domain, MD: Molecular Dynamics, DSM : sphingolipid, POPC: 1-palmitoyl-2-oleoylphosphatidylcholine), POPE: 1-palmitoyl-2-oleoylphosphatidylethanolamine), POPS: 1-palmitoyl-2-oleoylphosphatidylserine.

Introduction

The cystic fibrosis transmembrane conductance regulator (CFTR) protein is a chloride/bicarbonate channel whose dysfunction is the root cause of cystic fibrosis (CF), a life-shortening genetic disease that causes inflammation and infections in the lungs and pancreatic insufficiency [1]. As a member of the ATP-binding cassette (ABC) superfamily, CFTR has two transmembrane domains (TMDs) and two nucleotide-binding domains (NBDs) that assemble via multiple, dynamic interfaces. CFTR (ABCC7) is closely related to members of the ABCC family which, together with the ABCB family, form the type IV systems, according to the topology of the TMDs [2–4]. The core of type IV TMDs consists of six transmembrane helices (TMs), which extend widely into the cytoplasm to form intracellular loops (ILCs) terminated by coupling helices (CHs) that interact with NBDs. In the fully assembled architecture of type IV systems, the fourth and fifth TMs of each TMD swap into the other TMD, so that the second CHs interact with the NBDs in the opposite half of the transporter.

Nine ABCC proteins (ABCC1-6 and ABCC10-12) form a group of multidrug-resistance-associated proteins (MRPs), involved in chemotherapy resistance by translocating anticancer drugs out of the cells [5]. The closest paralog of CFTR, ABCC4, transports numerous organic anions including chemotherapeutic agents, as well as various endogenous molecules, including cyclic nucleotides, folic acid, ecoisanoids, urate, prostaglandins, leukotrienes and conjugated steroids [6]. Like other proteins of the ABCC family, CFTR possesses a N-terminal lasso motif (called linker L0 in “long” ABCC members, which possess an additional N-terminal membrane-spanning domain (TMD0)). This lasso/L0 is partly inserted in the membrane and embraces both TMDs [7,8]. The ABCC family also possesses long, disordered links between NBD1 and TMD2 (called the regulatory (R) domain in CFTR), the phosphorylation of which regulates function [9]. CFTR has however evolved from this ABCC mold to exhibit regulated (ATP-gated) anion channel activity by acquiring unique structural features (reviewed in [10]). The alternating access mechanism of ABCC transporters associated with an anionic substrate translocation pathway has thus evolved towards the construction of an anionic channel pore, in which both gates are degraded and the open pore conformation stabilized [11]. The specific structural features of human CFTR include an unusual conformation of the TM7-TM8 hairpin, in which unwinding (or discontinuity of the helical pattern) of a five amino acid long segment in TM8 leads to a displacement of the top of helix TM7 relative to its usual position on the extracellular side and gives rise to a pronounced asymmetry of the channel ([8] and reviewed in [12]). Another specific feature of CFTR is a “degenerated” intracellular gate, which is closed when the NBDs are in a dimerized state, but accompanied by an open lateral entrance (or portal) between TM4 and TM6 (TM4/TM6 portal), allowing anion flow from the cytoplasm to the inner vestibule. This

characteristic is attributable to the pronounced divergence of TM6, harboring a kink at the level of arginine ARG352, at which TM6 can move away from TM4 to create this portal at the basis of the intracellular loops. Of note is that a symmetric, secondary TM10/TM12 pore has been identified by two independent studies using molecular dynamics (MD) simulations on a human CFTR three-dimensional (3D) structure model [13] and on the experimental 3D structure of zebrafish CFTR [14], without being demonstrated experimentally by cryo-electron microscopy (cryo-EM) studies conducted to date. The static cryo-EM 3D structures of the phosphorylated, ATP-bound CFTR have also failed to elucidate the mechanism of complete opening of the channel at the extracellular end. Indeed, even in complex with the potentiator VX-770 (Ivacaftor) [15], these structures do not have a conduction pore passing through the entire thickness of the membrane, as this one is closed near the channel selectivity filter or, in one case [16], too narrow at this level to accommodate any other else than a fully dehydrated chloride ion.

Previous studies have enlightened the importance of a few electrostatic bonds (i.e. chemical bonds characterized by an electrostatic attraction) for stabilizing the open state of the CFTR channel. These involve $ARG352_{TM6}$ mentioned above, forming a salt-bridge with $ASP993_{TM9}$, but also $ARG347_{TM6}$ interacting with $ASP924_{TM8}$ (at the N-terminal extremity of TM8) [17–19]. The existence of these salt-bridges was supported by cryo-EM 3D structures of human CFTR, which revealed at this depth in the lipid bilayer an additional salt-bridge between $ARG933_{TM8}$ (at the C-terminal extremity of the TM8 unwound segment) and $GLU873_{TM7}$ [20]. Another salt bridge was also identified within the four-helix bundle linking the four ICLs, at the level of ICL2 ($GLU267_{TM4}$) and ILC4 ($LYS1060_{TM10}$), which directly influence channel gating [21,22]. Finally, a hydrogen bond has also been highlighted between the side chain of ARG117 (ExtraCellular Loop ECL1) and the backbone carbonyl group of $GLU1124_{ECL4}$, formed only in the open state of the channel [23,24].

Our aim here was to comprehensively analyze the full networks and dynamics of electrostatic bonds (salt-bridges and hydrogen bonds) between side chain atoms present in human CFTR, but also linking these side chains to ions and lipids. To that aim, we performed all-atom molecular dynamics (MD) simulations of the human CFTR 3D structure (phosphorylated, ATP-bound form), in the apo form and in the presence of the potentiator VX-770, embedded in a complex, asymmetric membrane bilayer. This analysis led to the identification of novel key partners, including some only revealed in our MD simulations (and not present in the cryo-EM 3D structure). These bonds may be critical either for the architecture of the channel or for regulating its activity, including via the potentiator VX-770, whose mechanisms of action remain incompletely understood. Finally, this study has enabled us to shed additional light on the specific evolution of CFTR with respect to other members of the ABCC family, probably linked to

the optimization of the gating mechanism. Altogether, this fundamental study may provide novel insights into how the open state of the channel may be induced and stabilized and ultimately, may help the design of novel potentiators.

Results

Overview of the MD simulations

For this study, we performed eight independent all-atom molecular dynamics (MD) simulations of the human CFTR 3D structure (ATP-bound) embedded in a heterogeneous lipid bilayer composed of the phospholipids phosphatidylcholine (POPC), phosphatidylethanolamine (POPE) and phosphatidylserine (POPS), together with cholesterol (CHL1) and the sphingolipid DSM, using proportions similar to those proposed by Domicevica and colleagues [25] (see Methods): four in the absence of ligand (apo conditions, labeled Apo1, Apo2, Apo3, Apo4) and four in the presence of the potentiator VX-770 (Ivacaftor) (ligand-bound conditions, VX1, VX2, VX3 and VX4). Each simulation was run for either 500 ns or 1000ns, yielding a total of 6 μs of simulation time. To further ensure the robustness of our results, we employed different thermostat–barostat combinations across the simulations (Nosé–Hoover / Parrinello–Rahman, V-rescale / C-rescale and Langevin dynamics; see Methods). This strategy allowed us to confirm that the observed behaviors were independent of the coupling scheme and thus not an artifact of a specific algorithm.

To evaluate the structural stability of the protein, we calculated the root-mean-square deviation (RMSD) of CFTR backbone atoms relative to the starting cryo-EM structure. As shown in **Figure S1**, all trajectories reached convergence within the first 100–200 ns, with RMSD values stabilizing between 2.5 and 3.5 Å, indicating stable overall protein conformations in both apo and ligand-bound conditions.

In parallel, we examined membrane behavior to ensure bilayer stability across all simulations. The area per lipid (APL) and membrane thickness were computed for each replica, as shown in **Figure S2**. These metrics remained stable throughout the simulations, with an area per lipid of approximately 62 Å² and an average membrane thickness of 45 Å, confirming that all systems remained equilibrated and structurally consistent. Compared to a pure POPC bilayer (thickness ~37 Å and with APL ~65 Å² in [26], the mixed bilayer appeared thicker. This observation is consistent with findings from other ABC transporters, such as P-glycoprotein, where POPE-containing systems produce more ordered bilayers (smaller APL and greater thickness [27]) and cholesterol-rich bilayers induce increased membrane thickness [28,29].

These MD simulations enabled reliable analysis of residue-level electrostatic interactions, as well as contacts with anion and lipid headgroups in both the apo and ligand

(VX-770)-bound conditions. These contacts were calculated using a rigorous, geometry-based definition of interatomic interactions, based on a tessellation method used by the VLDM (Voronoi Laguerre Delaunay for Macromolecules) program (see Methods). This geometrical approach, integrating all heavy atoms of the MD simulations including water, has the advantage of allowing for a comprehensive analysis of the entire system, without preconceptions and without imposing arbitrary distance cutoffs. Contacts are correlated to the presence of electrostatic bonds (salt bridges (SBs) and hydrogen bonds (HBs)), terms that will be used appropriately in cases supported by 3D structure inspection. From the analysis of the MD trajectories, we identified 799 electrostatic interactions between charged or polar side-chain atoms within CFTR's 3D structure. We included in our analysis basic (ARG, LYS, HIS) and acidic residues (ASP, GLU), as well as SER, THR, ASN, GLN, CYS, TYR and TRP. For TRP, the cation-π and π-π interactions (interactions between ARG and aromatic side chains) were not considered in the statistics of electrostatic interactions, but illustrated when associated with networks of electrostatic interactions. To focus on robust and functionally relevant interactions, we considered only bonds that formed for at least 10% of the total simulation time across all apo simulation replicates, resulting in a final set of 558 electrostatic interactions. The frequencies of these interactions are reported for each of the eight MD simulations in **Figures S3 to S4** (amino acids pairs, presented with the first amino acids of the pairs following the order of the polypeptide chain progression), while frequencies of contacts of polar/charged amino acids with ions and lipids are listed in **Figures S5 to S6**. We also recorded electrostatic interactions linking charged or polar side-chain atoms and main-chain atoms (738 contacts with frequencies above 10 % across all apo MD simulations). In the following chapters, we analyzed in detail the side-chain/side-chain networks, while only illustrating some notable features of the side-chain/main-chain networks.

Spatial distribution of CFTR electrostatic interactions and functional impact

Electrostatic interactions between side chain atoms were categorized by their location into five structural regions of CFTR, based on the average Z-coordinate of the involved residues (see Methods): (i) the extracellular loops (ECLs), (ii) the transmembrane (TM) helices (TM helices/Membrane), (iii) the membrane-proximal elbow and lasso regions along with the intracellular loops (Elbow/Lasso/ICLs), (iv) the ICLs-nucleotide-binding domains (ICLs/NBDs) interface and (v) the NBDs. **Figures S7A/B** illustrate the distribution of these contacts in each region, ordered by mean frequency, while **Figure 1** maps their spatial distribution on CFTR 3D structure where each residue is color-coded by its assigned structural region (red for ECLs, orange for TM helices/Membrane, yellow for elbow/lasso/ICL regions, green for ICLs/NBD interface and blue for NBDs). We then classified electrostatic interactions by whether the basic

amino acid or SER/THR/ASN/GLN/TYR/TRP partner simultaneously engaged in anion coordination (cyan in **Figure S8**), lipid binding (yellow), both (purple), or neither (light gray). Strikingly, over half of the frequent contacts in the ECLs, TM helices/Membrane, Elbow/Lasso/ICLs regions have dual functionality: many of the residues mentioned above, forming electrostatic interactions with other residues also served as binding sites for chloride or bicarbonate ions, membrane lipids, or both. This suggests that several non-covalent bonds in CFTR are components of larger electrostatic networks that link the protein's intramolecular contacts to its interactions with the membrane environment and anions.

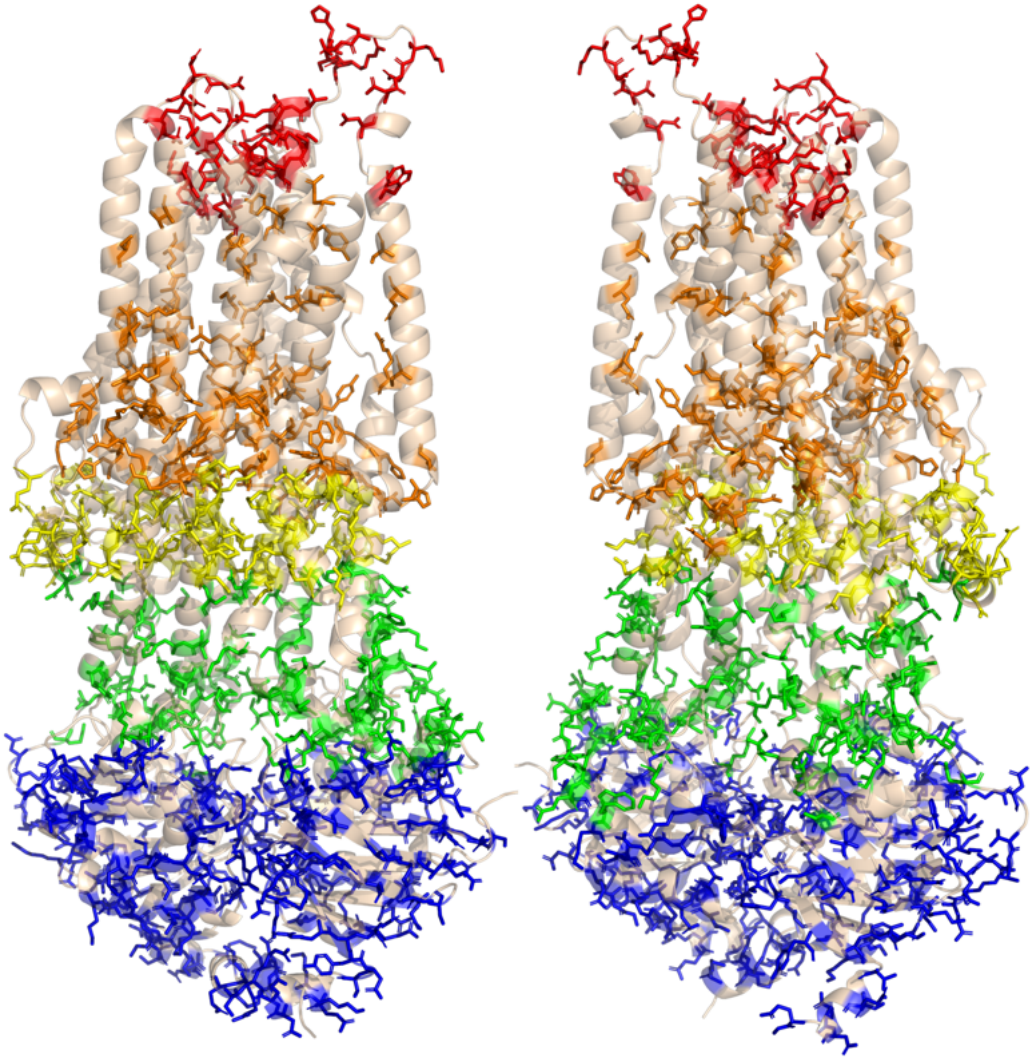

Figure 1: 3D mapping of CFTR residues involved in side-chain/side-chain electrostatic interactions. Two views of the human CFTR 3D cryo-EM structure (pdb 6O2P, 180° apart along the z-axis, ribbon representation), show the spatial distribution of residues engaged in electrostatic interactions (side-chain/side-chain contacts, mean frequencies > 10%). Residues are represented as sticks and color-coded according to their location on the 3D structure: red for ECLs, orange for transmembrane helices / membrane regions, yellow for elbow/lasso/top ICLs regions, green for the bottom ICLs–NBDs interface and blue for the NBDs. A coordinate-based scheme along the Z-axis was used to classify residues into these five structural regions (see Methods).

We then analyzed in detail these networks, region by region, starting from the extracellular side toward the cytoplasm.

In the **ECLs**, no highly stable interaction was observed between side chain atoms (mean frequencies below 0.6) (**Figures S7A/B**), reflecting the dynamic and solvent-exposed nature of the extracellular region. However, several transient intra- and inter-ECLs interactions are observed, involving more than 20 charged/polar amino acids from ECL1 and TM1/TM2 extracellular extremities (ARG104$_{TM1}$, SER108$_{TM1}$, TYR109$_{TM1}$, ASP110$_{ECL1}$, ASP112$_{ECL1}$, LYS114$_{ECL1}$, GLU116$_{ECL1}$, ARG117$_{ECL1}$), ECL3 and TM5/TM6 extracellular extremities (TYR325$_{TM5}$, LYS329$_{TM5}$, ARG334$_{TM6}$, THR338$_{TM6}$), ECL4 and TM7/TM8 extracellular extremities (ASP891$_{ECL4}$, LYS892$_{ECL4}$, SER895$_{ECL4}$, THR896$_{ECL4}$, HIS897$_{ECL4}$, ARG899$_{ECL4}$, THR908$_{ECL4}$, SER909$_{ECL4}$, THR910$_{ECL4}$, TYR913$_{TM8}$, TYR914$_{TM8}$) and ECL6 and TM11/TM12 extracellular extremities (THR1115$_{TM11}$, SER1118$_{TM11}$, THR1122$_{ECL6}$, GLU1124$_{ECL6}$, GLU1126$_{ECL6}$, ARG1128$_{ECL6}$, THR1134$_{TM12}$) (**Figures 2A** and **S7A/B**). ECL1, ECL3, ECL4 and ECL6 (colored in blue, green, yellow and red, respectively, in **Figure 2A**) form the core of the transmembrane assembly, while the remaining two shorter ECLs (ECL2 and ECL5, grey in **Figure 2A**), linking the four three-helix units (TM1-2-3, TM4-5-6, TM7-8-9 and TM10-11-12) [30], are located at the periphery of the transmembrane assembly. ASP110$_{ECL1}$, GLU116$_{ECL1}$ and ARG117$_{ECL1}$ have been shown to stabilize the open pore architecture [23]. The present study highlights that this contribution is likely due, for ASP110$_{ECL1}$, to transient interactions (HB) with LYS114$_{ECL1}$, THR910 $_{ECL4}$, as well as with ARG334$_{TM6}$ and TYR914$_{TM8}$ (both amino acids which also interact together and play a key role in controlling anion flux [23,31] and, for GLU116$_{ECL1}$, to transient interactions (SB) with the same ARG334$_{TM6}$. ASP110$_{ECL1}$ and GLU116$_{ECL1}$ thus belong to an intricate network of transient inter-ECL interactions located at the center of the ECL assembly, which also includes three tyrosine residues (TYR109$_{ECL1}$, TYR913$_{TM8}$ and TYR914$_{TM8}$) and other polar (THR910$_{ECL4}$, THR1134$_{TM12}$, SER1118$_{TM11}$) and charged (ARG334$_{TM6}$, ARG1128$_{ECL6}$) amino acids. With regards to ARG117$_{ECL1}$, a previously described HB with the backbone oxygen atom of GLU1124 $_{ECL6}$ reported by Simon and Csanády [24] was retrieved in our side-chain/main chain analysis (**Figure S7C/D**), in which ARG117 was observed to also establish HBs with main chain atoms of other amino acids from ECL1 (TYR109$_{TM1}$, ASP110$_{ECL1}$, PRO111$_{ECL1}$) and ECL6 (ILE1119$_{TM11}$, LEU1120$_{TM11}$, THR1121$_{ECL6}$, THR1122$_{ECL6}$, GLY1123$_{ECL6}$, GLU1124$_{ECL6}$, GLY1125$_{ECL6}$, GLY1127$_{ECL6}$). This tight network likely contributes to the stabilization of the ECL1 conformation. The most frequent side chain/main chain interactions involve ECL2 SER222$_{TM4}$, whose hydroxyl group makes HBs with the main chain nitrogen atom of ECL3 TYR325$_{TM5}$, while the same TYR325$_{TM5}$ hydroxyl group frequently interacts with the main chain oxygen atom of LEU218$_{ECL2}$. No such contact was detected for the symmetrical ECL5, which remains disconnected from the

transmembrane assembly. Another striking feature in this region is the HB network between ECL3 and ECL4 main chain atoms, leading to a short β-sheet, which likely contributes to stabilize the ECL assembly (**Figure 2A)**. Additionally, it is important to note that ECL4 is particularly long and is not fully resolved in current cryo-EM structures; therefore, it was modeled in our simulations to ensure the structural continuity and completeness required for the accurate representation of CFTR dynamics in this extracellular region. Finally, also of note is the transient HBs made by the three tyrosine residues described above (TYR109$_{ECL1}$, ECL4 TYR913$_{TM8}$ and TYR914$_{TM8}$) with main chains atoms of other ECLs, contributing to reinforce the central network (**Figures S7C/D**). Overall, the analysis of electrostatic interactions in the ECL region reveals an intricate and dynamic network in which several charged and polar amino acids play a central role.

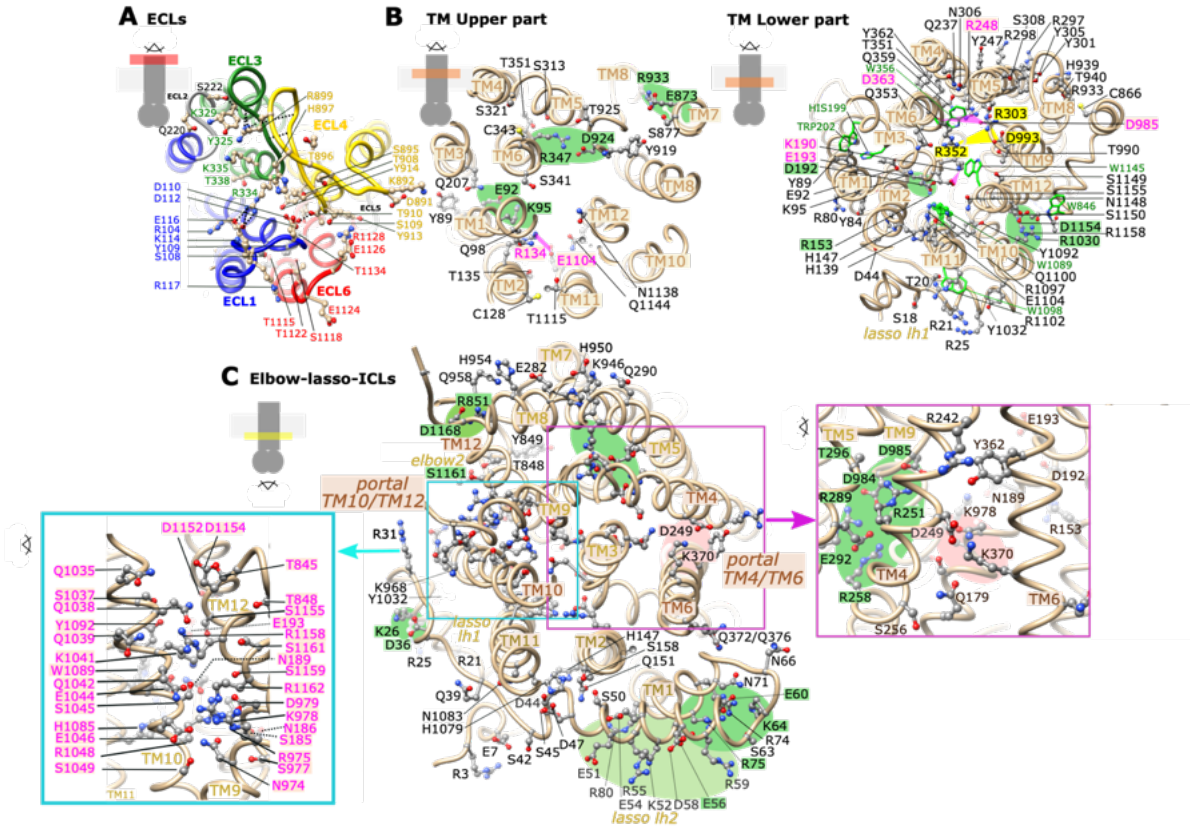

Figure 2: Electrostatic interactions in the transmembrane domains (TMDs) of CFTR. These interactions are visualized on the human CFTR 3D structure after 500 ns of MD simulation (apo condition, replica 1). **A) Within the ECLs** (region colored in red in Figure 1, view from the extracellular side). The charged/polar amino acids involved in electrostatic interactions, as listed in Figures S7A and S7B, are depicted in atomic details and colored according their belonging to ECL1 (blue), ECL3 (green), ECL4 (yellow) and ECL6 (red). **B) Within the membrane regions of the transmembrane domains** (region colored in orange in Figure 1, view from the extracellular side), in which electrostatic interactions are organized into two approximate layers. Highly stable salt-bridges are shown in green, while less stable ones are in pink. The particular case of bonds linking ASP993 to ARG303 and ARG352 is highlighted in yellow. TRP residues, which are mostly involved in cation-π interactions with ARG residues, are shown in green. **C) At the level of the Elbow-lasso-ICLs** (region colored in yellow in Figure 1, view from the intracellular side). The same colors as in panel B are used to highlight stable and transient salt-bridges.

In the **transmembrane (TM helices/Membrane) region**, five SBs were found to be highly stable (mean frequency > 80%) across simulations: ARG933$_{TM8}$–GLU873$_{TM7}$, ARG153$_{TM2}$–ASP192$_{TM3}$, ARG347$_{TM6}$–ASP924$_{TM8}$, ARG1030$_{TM10}$–ASP1154$_{TM12}$ and GLU92$_{TM1}$-LYS95$_{TM1}$ (intra-helix) (**Figure S7A;** highlighted in green in **Figure 2B**). The high stability of these SBs suggests a structural role in maintaining the integrity of the CFTR transmembrane architecture. Three of them (ARG933$_{TM8}$–GLU873$_{TM7}$, ARG347$_{TM6}$–ASP924$_{TM8}$ and ARG153$_{TM2}$–ASP192$_{TM3}$) are located in the vicinity of TM irregularities, involving TM8 (for which the unwound segment is surrounded in both sides by ASP924$_{TM8}$ and ARG933$_{TM8}$) and TM3, suggesting that they may be critical for maintaining such particular conformations (further discussed below). Of note is that the ARG347$_{TM6}$ and ARG933$_{TM8}$ side-chains are also involved in multiple HBs with main chain atoms (**Figure S7C)**, contributing to reinforce interactions in these regions. ARG347$_{TM6}$–ASP924$_{TM8}$, together with ARG352$_{TM6}$-ASP993$_{TM9}$ have been described as playing key roles in the channel function [17,18,32]. Interestingly, the ARG352$_{TM6}$-ASP993$_{TM9}$ SB, present in the cryo-EM 3D structure, appears to be far less stable (mean frequency <30 %), while ASP993$_{TM9}$ is more frequently salt-bridged with ARG303$_{TM5}$ (mean frequency ~70 %) (yellow shading in **Figure 2B**) . ARG303$_{TM5}$, ARG352$_{TM6}$ and LYS95$_{TM1}$ (from the cytosolic vestibule towards the upper part of the channel) are positioned along the channel pore. As for ARG303$_{TM5}$-ASP993$_{TM9}$-ARG352$_{TM6}$, all less stable SBs in the membrane region (pink in **Figure 2B**) including ASP363$_{TM6}$–ARG248$_{TM4}$–ASP985$_{TM9}$ (upper part of the TM4/TM6 portal), GLU193$_{TM3}$–LYS190$_{TM3}$-ASP363$_{TM6}$ (cytoplasmic vestibule), and ARG134$_{TM2}$–GLU1104$_{TM11}$ (upper part of the channel), were found to engage in anion contacts, supporting a potential relationship between reduced salt bridge stability and functional involvement in anion interactions through electrostatic interactions.

In contrast, the stable SB ARG1030$_{TM10}$-ASP1154$_{TM12}$ (green in **Figure 2B**) is located at the periphery of the membrane assembly, more precisely at the top of the potential TM10/TM12 portal, and appears accessible to lipid headgroups. Notably, only one SB in this region, ARG1158$_{TM12}$–ASP1154$_{TM12}$, was found to have both anion and lipid contacts (**Figure S8**), although with very low frequency. Its strategic position in the upper part of the TM10/TM12 portal may reflect a dual role in membrane coupling and ion conduction. Finally, two HBs linking amino acids from TM11 and TM12 (GLN1100$_{TM11}$-ASN1148$_{TM12}$ and TYR1092$_{TM11}$-SER1155$_{TM12}$) are among the most stable ones (**Figure S7B**), suggesting that these may be involved in the proper positioning of the swapped TM10-TM11 hairpin carrying the ICL4 coupling helix, which contacts NBD1. Another stable HB (GLN237$_{TM4}$-ASN306$_{TM5}$) links amino acids from the swapped TM4-TM5 hairpin (carrying ICL2), suggesting a key role in its packing. In conclusion, the lower part of the TMD concentrates a large number of electrostatic interactions (SBs and HBs), forming dense networks and involving amino acids from all the TMs, except TM7. Moreover, several TRP residues are found in this region, making cation-π interactions with ARG involved in SBs,

thereby strengthening the bond networks (**Figure S7B**). For instance, TRP1098$_{TM11}$ forms a highly stable contact with ARG1102$_{TM11,}$ TRP356$_{TM6}$ makes frequent contacts with ARG303$_{TM5}$ and ARG352$_{TM6}$, while TRP1089$_{TM11}$ frequently contacts both ARG153$_{TM2}$ (cation-π) and ASP192 $_{TM3}$ (HB). Also of note at this level, the stable contact between HIS199$_{TM3}$ and TRP202$_{TM3}$, both amino acids belonging to an hydrophobic pocket at the TMD1 surface, which interacts with the correctors VX-809 (Lumacaftor) and VX-661 (Tezacafor) [33,34].

In the **Elbow/Lasso/ICLs region**, including the inner vestibule and lateral portals, ten SBs exhibited high stability (mean frequency > 80%) (**Figures 2C and S7A**). Among them, the network involving ARG258$_{TM4}$–GLU292$_{TM5}$–ARG289$_{TM5}$–ASP984$_{TM9}$ appears to serve a purely structural role, as no electrostatic interactions with ions or lipids were detected (**Figure S8**). Similarly, the SBs GLU56$_{lh2}$–ARG75$_{elbow1}$–GLU60$_{lh2}$–LYS64$_{lasso}$ (and HBs of ASN71$_{elbow1}$ with GLU60$_{lh2}$, LYS64$_{lasso}$ and ARG74$_{elbow1}$ **Figure S7B**) and LYS26$_{lh1}$–ASP36$_{lasso}$, located within the lasso region *(lh1 and lh2 refers to lasso helix 1 and 2)*, are likely important for structural integrity of this domain and membrane insertion, with electrostatic interaction with lipids (**Figure S8**). In contrast, THR296$_{TM5}$-ARG251$_{TM4}$–ASP985$_{TM9}$, in continuity of the network described before, is both highly stable and engaged in anion contact, suggesting a dual structural and functional role in anion conduction (**Figure S8**). Another highly stable SB, linking the elbow preceding TMD2 (ARG851) and the end of TM12 (ASP1168), appears to play a key structural role in the membrane anchoring of TMD2 via electrostatic interactions established with lipids.

Several less frequent electrostatic interactions in this region appear to form a tightly interconnected network that is prominently involved in anion conduction (**Figure 2C**). These include LYS1041$_{TM10}$–GLU1044$_{TM10}$–ARG1048$_{TM10}$–SER1045$_{TM10}$-ARG1162$_{TM12}$-ASP979$_{TM9}$, as well as SER1045$_{TM10}$–ARG975$_{TM9}$–ASP979$_{TM9}$–ARG1048$_{TM10}$-SER1159$_{TM12}$-LYS1041$_{TM10}$, GLU1046$_{TM10}$-SER1045-ASP979$_{TM9}$–SER1159$_{TM12}$-GLU1044$_{TM10}$-SER1045$_{TM10}$, and SER1049$_{TM10}$-ARG975$_{TM9}$–GLU1046$_{TM10}$–ARG1162$_{TM12}$–SER1045$_{TM10}$. This network integrates several asparagine (ASN189$_{TM3}$ and ASN974$_{TM9}$) and glutamine (GLN1035$_{TM10}$, GLN1038$_{TM10}$ and GLN1042$_{TM10}$) (**Figure S7B)**, whose amide groups may act simultaneously as hydrogen bond donors and acceptors. Of note is the most stable HB linking the GLN1038$_{TM10}$ and ARG1158$_{TM12}$ side chains. These residues form an extended network spanning TM9, TM10, TM12, and the intracellular loops, converging around a region accessible to the intracellular vestibule and involved in gating or coordination of anions. The recurrence of overlapping residues across multiple interactions and the presence of several charged and polar residues within this cluster suggest a cooperative mechanism, where dynamic bond switching may modulate local electrostatics and facilitate anion conduction or structural flexibility in this critical intracellular region. Importantly, this network also extends to the TM10/TM12 portal, further supporting its role as a central hub for anion accommodation and electrostatic coupling. As for

membrane regions, several HBs are observed linking side-chain to main-chain atoms in the vicinity of side-chain/side-chain bonds (**Figure S7C/D**), therefore contributing to reinforce the observed networks.

In the lasso region (**Figure 2C**), upstream of the first elbow, a large network of electrostatic interactions is also involved in both membrane and anion interactions. These include SER63$_{lh2}$–ARG59$_{lh2}$–GLU56$_{lh2}$–LYS52$_{lh2}$ and ASP58$_{lh2}$–ARG55$_{lh2}$–GLU51$_{lh2}$, as well as GLU54$_{lh2}$–ARG55$_{lh2}$–GLU56$_{lh2}$. Such interactions may contribute to membrane insertion and anchoring, while also attracting ions.

Other less frequent SBs in this region, such as LYS370$_{TM6}$–ASP249$_{TM4}$ located at the entrance of the TM4/TM6 portal (a known access route for anions), do not exhibit contacts with lipids or anions (**Figure 2C**). The relatively low stability of this particular SB (and the proximal HB between TYR362$_{TM6}$ and ARG242$_{TM4}$) raises the question of whether it plays a transient or conditional role in stabilizing the portal architecture, potentially responsive to conformational shifts or binding events.

At the **ICLs/NBDs interface** (**Figures 3A and S7A/B**), SBs and HBs linking side chains appear to play primarily a structural role, as none was observed to participate in anion or lipid headgroup interactions. This suggests that their main role is to stabilize the coupling between the TMDs and the NBDs, in particular through amino acids belonging to the ICLs coupling helices (CHs). The most stable bonds networks in this region, connecting TMDs to NBDs, include SER169$_{CH1}$–ARG1066$_{CH4}$–GLU474$_{NBD1}$, LYS273$_{CH2}$–GLU1172$_{TMD2\text{-}NBD2\ linker}$–ARG1283$_{NBD2}$, LYS163$_{TM2}$–GLU379$_{TMD1\text{-}NBD1\ linker}$ and CYS1355$_{NBD2}$-TYR275$_{CH2}$. These bonds, located at the periphery of the CFTR domain assembly, likely act as buttresses, helping to maintain the proper alignment and communication between intracellular loops and the NBDs. The importance of ARG1066$_{CH4}$ in the CFTR multidomain assembly is supported by the fact that mutations of this amino acid in CF patients (p.Arg1066His and pArg1066Cys) are associated with a severe class II defect, which is rescued by ETI (Elexacaftor (VX-445), Tezacaftor (VX-661), Ivacaftor (VX-770)) therapy [35]. Furthermore, always at the ICL4 level, there are multiple HBs between arginine side chain atoms (ARG1066$_{CH4}$, ARG1070$_{TM11}$) and main chain atoms, including a very stable one between ARG1070$_{TM11}$ and PHE508$_{NBD1}$ (**Figure S7C**). This tight network of electrostatic interactions, including amino acids from ICL1, ICL4 and NBD1 but also from the TMD1-NBD1 linker (GLU379 and LYS381), is located at the level of the non-canonical/degenerate ATP-binding site (accommodating ATP(A) in **Figure 3A**), at which prolonged ATP retention is observed [36,37]. A tight network also exists at the ICL2:ICL3:NBD2 interface, including two cysteine residues (CYS276$_{CH2}$ and CYS1355$_{NBD2}$), which stably interact with the side chain of GLN1280$_{NBD2}$ and TYR275$_{CH2}$, respectively. As for the ICL1:ICL4:NBD1

interface, the network also includes an amino acid of the TMD2-NBD2 linker (GLU1172), and integrates several HBs established between side and main chain atoms (**Figure S7C/D**).

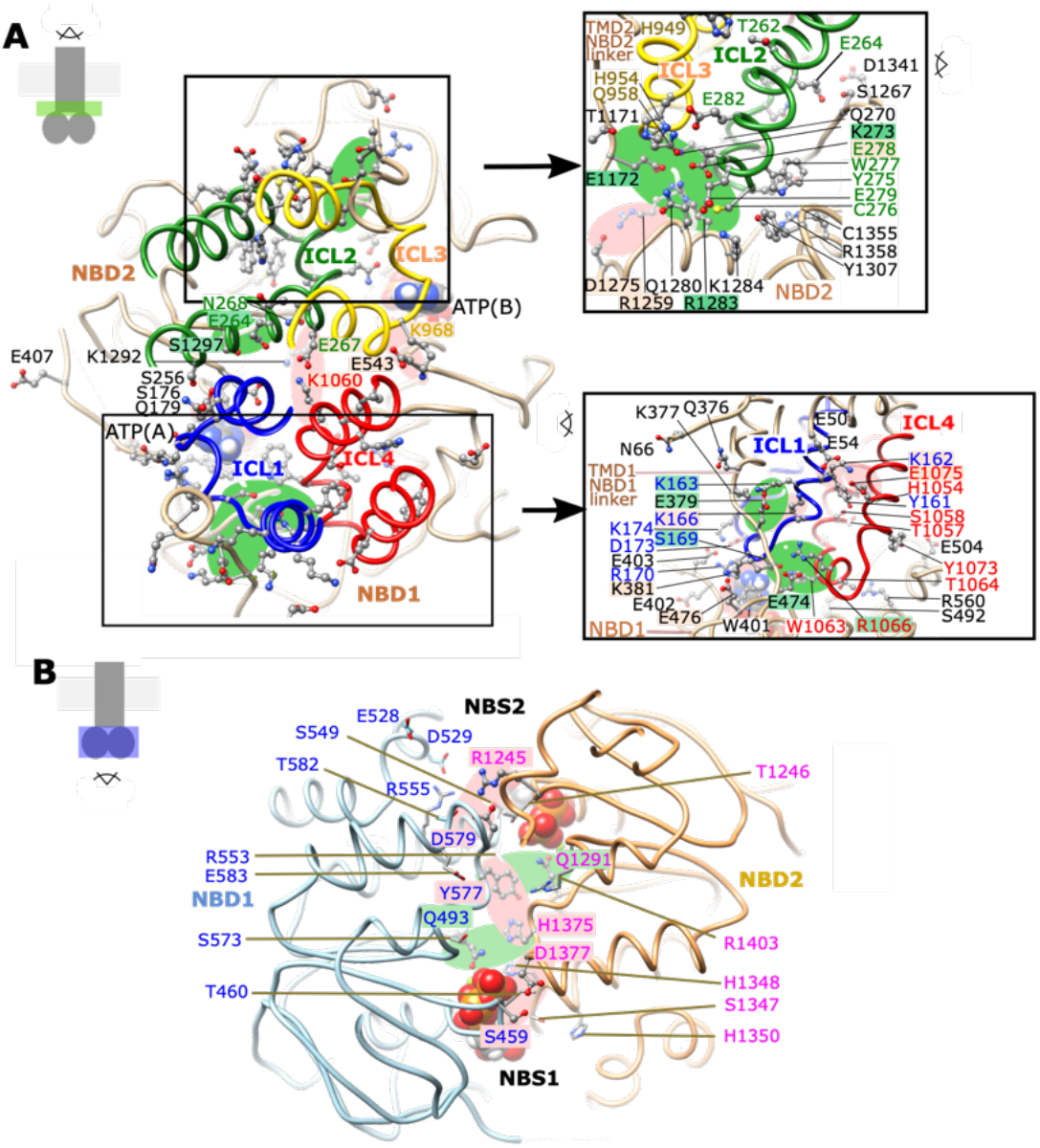

Figure 3. Electrostatic interactions at the ICLs:NBDs interface (A) and at the NBD1:NBD2 interface (B). These interactions, visualized on the human CFTR 3D structure after 500 ns of MD simulation (apo condition, replica 1), are extracted from regions colored in green (A, viewed from the extracellular side) and blue (B, view from the intracellular side) in Figure 1. **A)** Highly stable interactions between charged amino acids are shown in green and less stable contacts are in pink. **B)** Electrostatic interactions linking NBD1 (blue) and NBD2 (orange). ATP (spheres) is bound at both nucleotide-binding sites (NBS1 - bottom and NBS2 - top).

Several additional electrostatic interactions exhibited intermediate stability (mean frequency between 50% and 80%), including LYS1060$_{TM10}$–GLU267$_{TM4}$, LYS968$_{CH3}$–GLU543$_{NBD1}$, LYS162$_{TM2}$–GLU1075$_{TM11}$, ARG1283$_{NBD2}$–GLU278$_{TM5}$, LYS381$_{TMD1\text{-}NBD1\ linker}$–GLU476$_{NBD1}$, GLU264$_{TM4}$–SER1297$_{NBD2}$ and LYS166$_{ICL1}$–GLU379$_{TMD1\text{-}NBD1\ linker}$. These moderately stable interactions likely contribute to dynamic structural adjustments that support the conformational transitions

required for CFTR function while maintaining sufficient anchoring of intracellular elements. Of note is the central $LYS1060_{TM10}$–$GLU267_{TM4}$ SB, at the very C-terminal ends of TM10 and TM4, which helps to maintain the ICL four-helix bundle assembly and was previously shown to be critical for the CFTR function [21,22].

In the **NBDs**, numerous bonds were identified, with a noticeably higher concentration within NBD1 compared to NBD2 (**Figures S7A/B**). Interestingly, the majority of these bonds exhibited low stability, with approximately two-thirds showing mean frequencies below 50%. This may reflect the inherent flexibility of the NBDs and their dynamic behavior during the ATP-binding and hydrolysis cycle. The lower stability of these bonds could also suggest a more transient regulatory or allosteric role rather than a purely structural function. This regional asymmetry in electrostatic interactions distribution and stability may be linked to the non-equivalence of NBD1 and NBD2 in CFTR's transport mechanism [38,39].
Several bonds bridging NBD1 and NBD2 exhibited moderate stability (mean frequency >50%) (**Figures 3B** and **S7A/B**). The two first ones ($SER459_{NBD1}$–$ASP1377_{NBD2}$ and $ARG1245_{NBD2}$–$ASP579_{NBD1}$) involve two homologous pairs of amino acids: on the one hand, the two aspartic acids of the D-loop and, on the other hand, two amino acids preceding the Walker A motif. Three other ones involve two homologous amino acids ($TYR577_{NBD1}$ and $HIS1375_{NBD2}$) located two residues upstream of the D-loop aspartic acids and which interact either together or with the two Q-loop glutamine residues of the opposite NBD ($GLN1291_{NBD2}$ and $GLN493_{NBD1}$). In ABC transporters, the position of these two homologous amino acids located in the center of the dimer interface are generally occupied by small amino acids (GLY, ALA, SER), except for CFTR ($TYR577_{NBD1}$ and $HIS1375_{NBD2}$) and for members of the ABCE (TYR) and ABCF (HIS, ASN, MET) families [37]. A dozen other bonds also contribute to these interdomain interactions, distributed all along the NBD dimer interface (**Figure 3B**), among which the one comprising $HIS1348_{NBD2}$ (the first histidine of the degenerate (LSHGH) ABC signature) forming an alternative bond with $GLN493_{NBD1}$ to that established with $HIS1375_{NBD2}$. All these bonds may contribute to maintain the dimer interface alignment or to facilitate proper conformational transitions during ATP hydrolysis. Notably, their moderate stability could reflect a balance between the need for dynamic dissociation (during NBD opening) and transient stabilization (during dimer formation), underscoring a potential mechanistic role in the gating cycle of CFTR. The D-loop has been shown in several ABC transporters to play a central role in mediating allosteric communication between the two nucleotide-binding sites (NBSs), thereby regulating NBD dimer dynamics and ATP hydrolysis. It is suggested to play asymmetric roles, with the consensus site D-loop being essential for ATP hydrolysis, while the degenerate site D-loop stabilizes the NBD conformation [37,40]. Strikingly, most of these inter-NBDs bonds were only captured by MD and were not formed in the cryo-EM structures of CFTR (**Figure S9**),

suggesting their transient or state-dependent nature and pointing to a subtle but possibly critical mechanism for aligning the NBD dimer during the gating cycle.

Mapping of selective ion and lipid contact sites across CFTR

We then analyzed contacts of charged or polar atoms from ARG, LYS, HIS, SER, THR, ASN, GLN, TYR, TRP with anions (chloride and bicarbonate) and with lipid headgroups in each MD simulation replica in the apo conditions (**Figures 4 and S10, S11**).

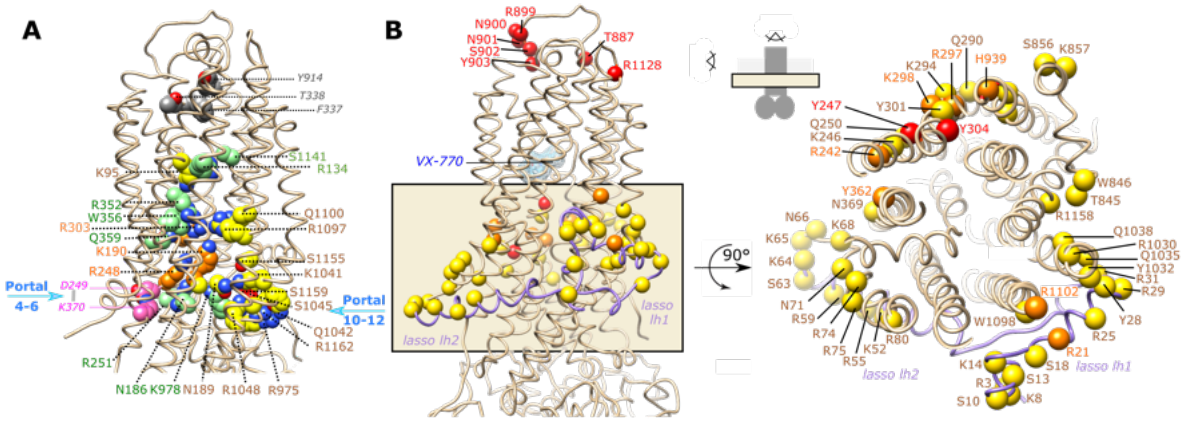

Figure 4: Electrostatic interactions with ions (A) and lipids (B). These interactions are visualized on the human CFTR 3D structure after 500 ns of MD simulation (apo condition, replica 1). In panel **A**, the carbon atoms of basic and polar side chains involved in electrostatic interactions with ions (chloride and bicarbonate) are represented in orange (most frequent ones) and green, whereas those of residues involved in specific interactions with chloride ions are shown in yellow. LYS370$_{TM6}$ and ASP249$_{TM4}$, which form a transient salt-bridge at the entrance of the portal 4-6, are shown in magenta. Amino acids of the dehydrated ion binding site (selectivity filter) identified by [16] in the upper part of the channel (T338$_{TM6}$, F337$_{TM6}$ and Y914$_{TM8}$) are colored in gray. For clarity purpose, the lasso is not represented in this view. In panel **B**, Cα atoms of basic and polar side chains involved in electrostatic interactions with POPS are represented in yellow, whereas specific interactions with cholesterol are shown in orange and red (depending on whether they overlap or not POPS binding sites, respectively). Two orthogonal views are provided, with the cross section seen from the transmembrane region.

For anions (**Figures 4A and S10**), the three most frequent contact sites with both chloride and bicarbonate ions are ARG303$_{TM5}$, ARG248$_{TM4}$ and LYS190$_{TM3}$ (orange in **Figure 4A**). The initial attraction typically occurs at ARG248$_{TM4}$, which likely serves as the primary entry point for anions through the portal displayed between TM4 and TM6 (TM4/TM6 portal), which is stably open in our MD simulations (**Figures 5A/C**). The ion may be then coordinated in the inner vestibule by ARG251$_{TM4}$ and/or LYS190$_{TM3}$, (with the participation of LYS978$_{TM9}$ and ASN186$_{TM3}$), afterwards transferred to ARG303$_{TM5}$ and to ARG352$_{TM6}$, positioned higher along the channel axis (with also, at this level, the participation of TRP356$_{TM6}$ and GLN359$_{TM6}$) and ultimately to LYS95$_{TM1}$ (with, at this level, the participation of ARG134$_{TM2}$ and SER1141$_{TM12}$) (**Figure 4A**). ARG1097$_{TM11}$ and ARG1100$_{TM11}$, facing ARG352$_{TM6}$, are also involved in specific interactions with chloride ions. The TM4–TM6 region consistently emerges as the most frequent and accessible anion entry pathway in our simulations. Residues identified here at TM4/TM6 portal

and in the central conduction pore are consistent with the results obtained from mutagenesis experiments [41–43]. However, it should be noted that LYS370$_{TM4}$, at the entrance of the TM4/TM6 portal, was not detected here in the group of anion binding residues, while it is involved in a transient SB with ASP249$_{TM4}$ (**Figure 2C**). This suggests that this interaction plays an essential role in regulating the anion flux. Interestingly, the formation of this ASP249$_{TM4}$-LYS370$_{TM6}$ SB divides the TM4/TM6 portal into two distinct, smaller portals (**Figure 5A**), suggesting that breakage of the bond could be associated with a higher ion flux.

Amino acids that specifically bind chloride ions (yellow on **Figure 4A**) are mostly found on the opposite side of the TM4/TM6 portal, at the level of the TM10/TM12 portal. The most frequent interaction occurs with LYS1041$_{TM10}$ and ARG1048$_{TM10}$, with involvement at the entrance of the portal of ARG1162$_{TM12}$, GLN1042$_{TM10}$, ARG975$_{TM9}$, and deeper towards to intracellular vestibule SER1045$_{TM10}$, SER1155$_{TM12}$, SER1159$_{TM12}$ and ASN189$_{TM3}$. Opening of this portal is repeatedly observed during our MD simulations (**Figures 5A/C**). Remarkably, all these conduction-related residues were also involved in SB/HB.

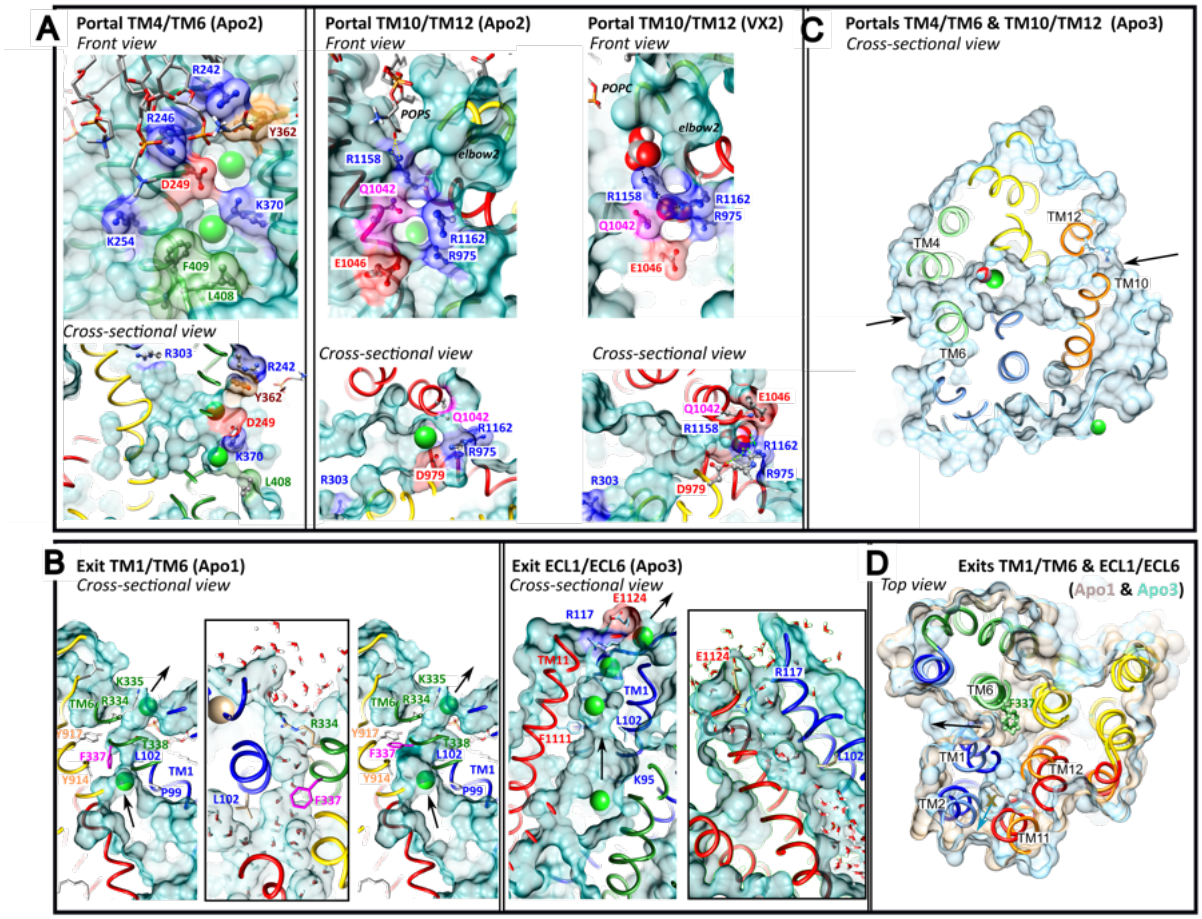

Figure 5: Views of the CFTR portals and exits. (**A-B**) The solvent-accessible surfaces (last frame of MD simulations) are represented, illustrating the topologies of the portals (**A**, front and cross-sectional views) and the extracellular exits (**B**, cross-sectional views). Chloride ions (green) were positioned along the pore to visualize the conduction paths, except for the portal TM10/12 (VX2 MD simulation) for which bound bicarbonate ions are shown. For the extracellular exits (B), the boxed views show the water molecules

within the conduction paths. For the exit TM1/TM6 (Apo1), the right-hand view illustrates the widening of the path at the selectivity filter following an alternative F337 rotamer. (**C-D**) General topologies of the portals (C) and exits (D), shown on different replica of MD simulations (Apo states, superimposed last frames). The ECL1-ECL6 exit is only open in the Apo3 MD simulation, while closed in the Apo1 one (closure symbolized with a cross).

We next examined the lipid selectivity of charged or polar atoms from ARG, LYS, HIS, SER, THR, ASN, GLN, TYR, TRP by specifically analyzing their interactions with cholesterol and phosphatidylserine (POPS), as these two lipids have been shown to have a direct influence on the intrinsic CFTR activity [44–46]. Distinct spatial patterns of lipid binding were observed across the protein (**Figures 4B and S11**). Cholesterol contacts were concentrated at specific sites (red/orange in **Figure 4B**), with the most consistent and frequent interactions observed with HIS939$_{TM8}$, TYR247$_{TM4}$, ARG242$_{TM4}$ and, to a lesser extent TYR362$_{TM6}$, which are positioned in the vicinity of the VX-770 binding site and form a potential cholesterol-mediated bridge to this site, suggesting a structural or allosteric communication role for this region. Just below the VX-770-binding site, a weaker but spatially aligned cholesterol interaction was also detected involving ARG297$_{TM5}$ and LYS298$_{TM5}$, further supporting the notion that this area may play a role in signal transmission between the drug-binding site and the TM helices mediated by the membrane. Finally, weak contacts with cholesterol were also observed for TYR304$_{TM5}$, which belongs to the VX-770 binding site. In the apo conditions, we also observed cholesterol contacts at ASN901$_{ECL4}$, SER902$_{ECL4}$, with lower-frequency interactions involving ARG1128$_{ECL6}$ (one replica), TYR903$_{ECL4}$, THR887$_{ECL4}$, ARG899$_{ECL4}$ and ASN900$_{ECL4}$ in the same region. Additional frequent contacts were detected in the lasso domain with ARG21$_{lh1}$. Interestingly, ARG1102$_{TM11}$, located near this lasso region and involved in the VX-445 (Elexacaftor)-binding site [47], also showed occasional cholesterol binding. Altogether, these observations suggest that cholesterol may contribute to the stabilization of the membrane insertion of the elbow and lasso domains, and to the regulation of the cytoplasmic-facing transmembrane helices involved in CFTR gating and/or allosteric regulation.

In contrast to cholesterol, POPS-binding residues (yellow and orange in **Figure 4B**) were more widely distributed and exhibited generally higher contact frequencies. Interestingly, several of the most significant POPS-binding regions overlapped with cholesterol-binding sites (orange in **Figure 4B)**. Prominent contacts were found within the lasso, notably at ARG25$_{lh1}$ and ARG21$_{lh1}$, with additional contributions from ARG29$_{lh1}$, SER18$_{lasso}$ and LYS14$_{lasso}$. ARG1102$_{TM11}$, located near this interface, also interacted with POPS, forming an extended functional lipid interaction zone. Another prominent POPS-binding site was identified in TM5 (LYS294, ARG297, LYS298) and TM4 (ARG242, LYS246), at the level of the headgroup region of the inner membrane leaflet, proximate to the VX-770 binding site, previously suggested to play a role in allosteric communication. POPS contacts were also observed here with HIS939$_{TM8}$.

The elbow region also displayed strong POPS contacts, particularly through ARG75$_{elbow1}$, while neighboring residues in the elbow-lasso interface—such as LYS52$_{lh1}$, ARG55$_{lh1}$, ARG59$_{lh1}$, LYS64$_{lasso}$, LYS65$_{lasso}$, ASN66$_{lasso}$, LYS68 $_{lasso}$, ARG74$_{elbow1}$ and ASN71$_{elbow1}$. ARG80$_{TM1}$ also contributed to significant contacts with POPS also found in interaction with the lasso at the level of LYS14$_{lasso}$. Notably, ARG1030$_{TM10}$ and ARG1158$_{TM12}$, together with THR845$_{elbow2}$, TRP846$_{elbow2}$, GLN1035$_{TM10}$ and GLN1038$_{TM10}$ also contacted POPS, despite not being involved in cholesterol interactions, pointing to distinct lipid specificity in this region. Overall, the distribution of POPS interactions appeared asymmetric, concentrated mainly on the NBD1-facing side of the CFTR structure, driven by substantial involvement of the lasso and elbow1 regions. This asymmetric lipid binding pattern may play a role in anchoring or orienting CFTR in the membrane and modulating region-specific conformational dynamics.

In conclusion, lipid interactions across CFTR were not random but instead revealed organized patches of lipid selectivity, with certain residues and structural domains preferentially recognizing specific lipid types. These findings underscore the relevance of CFTR's lipid-facing basic and polar residues in mediating membrane stabilization, potentially influencing conformational dynamics and coupling with ion transport.

Coupling TM helix irregularities to non-covalent interactions

We next examined whether the identified electrostatic interactions (SBs and HBs) correlate with local secondary structure features, focusing on irregularities within the TM helices and their behavior during MD simulations. **Table S2** lists the amino acids which exhibited transient or persistent deviations from an ideal helical geometry, defined as maintaining less than 80% α-helix occupancy throughout the MD simulations (α-helix occupancy is indicated for each MD simulation). These regions (blue ribbons in **Figure 6**) include charged and polar residues, whose side chains are all involved in electrostatic contacts (see the interaction partners in **Table S2**), accounting for approximately 10.4% of all detected interactions and ~22.9% of those located in the TM helices. Several of the affected residues also participated in contacts with anions, as specified in **Table S2**. Remarkably, these residues cluster into two distinct regions (encircled in **Figure 6**), *i.e.* the region around the TM8 unwound segment and a region located at the level of the internal vestibule and portals, with a particularly pronounced deformation of TM3 and TM9 (inset in **Figure 6**). Thus, residues located in helix irregularities often coincided with electrostatic contacts. In other words, when a charged amino acid side chain reaches out to form a SB, an alpha-helix can locally unwind or kink to accommodate that interaction.

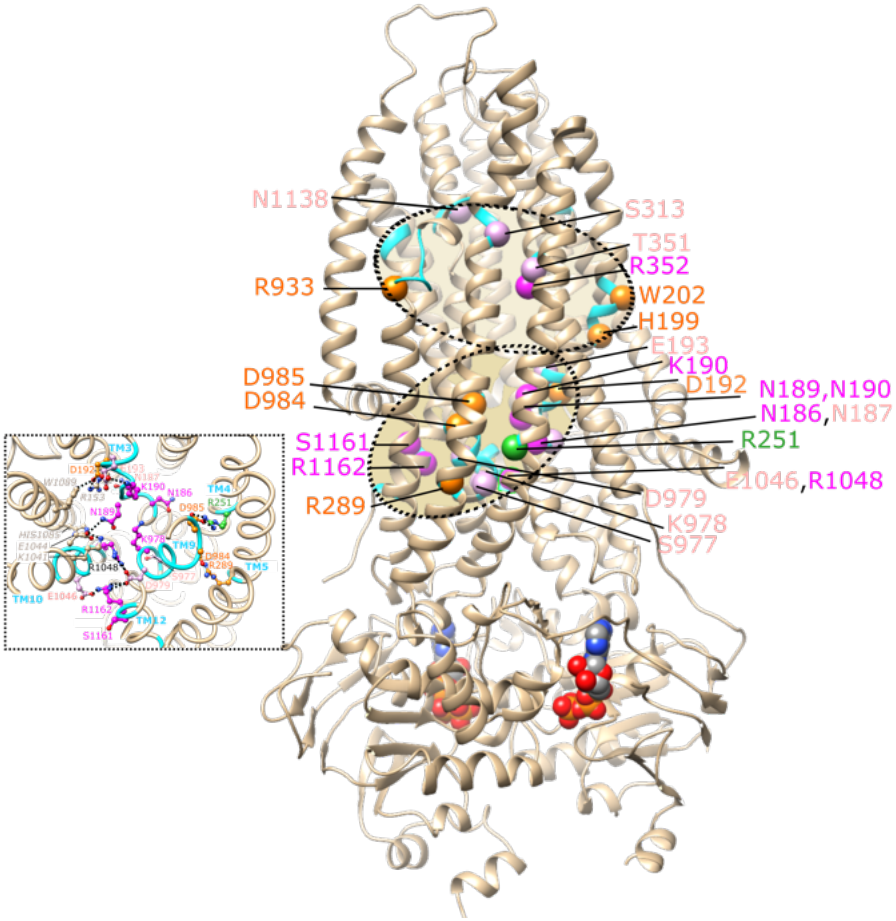

Figure 6: Charged and polar side chains involved in TM α-helix irregularities. The Cα atom positions of charged and polar residues included in α-helix irregularities, presented in **Table S2**, were mapped on the human CFTR 3D structure after 500 ns of MD simulation (apo condition, replica 1). They are colored according to their participation in stable or transient electrostatic interactions and in contacts with anions (stable interactions, with (green) or without (orange) contact with anions, transient interactions, with (magenta) or without (pink) contact with anions)). These residues cluster into two distinct regions (tan shaded), with that corresponding to the inner vestibule depicted in more details in the inset (amino acids involved in the interaction network but outside irregularities are depicted in grey).

A notable observation is that electrostatic interactions associated with anion contacts and integrating such local irregularities were almost always less stable (mean frequency < 80%), with the exception of the highly stable ARG251$_{TM4}$–ASP985$_{TM5}$ pair (98%), which engages in anion binding (yellow in **Figure 6**). Conversely, several SBs that do not participate in any anion interactions exhibited very high stability, often above 98% - notably ARG153$_{TM2}$–ASP192$_{TM3}$, ARG289$_{TM5}$–GLU292$_{TM5}$, ARG289$_{TM5}$–ASP984$_{TM9}$, and ARG933$_{TM9}$–GLU873$_{TM7}$ — suggesting a purely structural role. Interestingly, HBs involving SER or ASN displayed frequencies below 70%, supporting the idea that they contribute to more transient or flexible interactions. Taken together, these observations suggest a trade-off between stability and functional adaptability,

on a framework where the helices adapt by deviating locally from the alpha-helical pattern: highly stable electrostatic interactions may reinforce CFTR architecture, while less stable, dynamically switching interactions may support functional tasks like ion coordination or membrane coupling. Overall, integrating the secondary structure analysis with our interaction data highlights some residues as multi-faceted hubs where structure and function intersect: they are loci of helix deformability, intra-protein anchoring, and external ion/lipid engagement, all of which may be critical for CFTR's mechanistic flexibility.

Impact of VX-770 binding on electrostatic interactions

The cryo-EM 3D structure of human CFTR in complex with the potentiator Ivacaftor (VX-770) has highlighted a binding site at the protein-lipid interface, docked into a cleft formed by transmembrane helices TM4, TM5 and TM8, and involving the unwound segment of TM8 [15]. The binding pocket mainly involves aromatic and aliphatic hydrophobic residues. Our MD simulations highlighted the participation of lipids in the stabilization of the drug into the binding site. Most of the key interactions observed in the cryo-EM 3D structure were conserved during all the MD simulations, involving TM4 ($PHE236_{TM4}$), TM5 ($TYR304_{TM5}$, $PHE305_{TM5}$, $SER308_{TM5}$, $ALA309_{TM5}$ and $PHE312_{TM5}$) and TM8 ($GLY930_{TM8}$, $PHE931_{TM8}$ and $PHE932_{TM8}$) (**Figures 7A (**highlighted in green) and **7B**). Lower-frequency or conditional contacts (detected in only one of the simulations) included $PHE229_{TM4}$, $LEU233_{TM4}$, $GLN237_{TM4}$ and $LEU240_{TM4}$; $ASN306_{TM5}$ and $PHE316_{TM5}$; $ILE869_{TM7}$, $ALA876_{TM7}$ and $SER877_{TM7}$; $ALA928_{TM8}$, $LEU926_{TM8}$ and $MET929_{TM8}$. In one of the MD simulations (VX1), VX-770 slightly shifts towards TM7, establishing novel contacts with $GLU873_{TM7}$ (HB with VX-770 H9), which forms a strong SB with $ARG933_{TM8}$. This $ARG933_{TM8}$–$GLU873_{TM7}$ SB appears thus to serve a dual function: stabilizing the architecture of the binding pocket (including the unwound segment of TM8) and directly contributing to ligand binding and stabilization. Our MD simulations also revealed a striking effect of VX-770 on the structural integrity of TM8. In all the trajectories in the presence of VX-770, the region spanning $GLY930_{TM8}$ to $ARG933_{TM8}$ consistently maintained a stable helical conformation, whereas in all Apo simulations, this segment displayed clear irregularities and a tendency to unwind (**Table S2**). This observation suggests that VX-770 not only anchors within the TM8 cleft but also contributes to stabilize the local secondary structure, thereby potentially supporting its role in CFTR gating modulation.

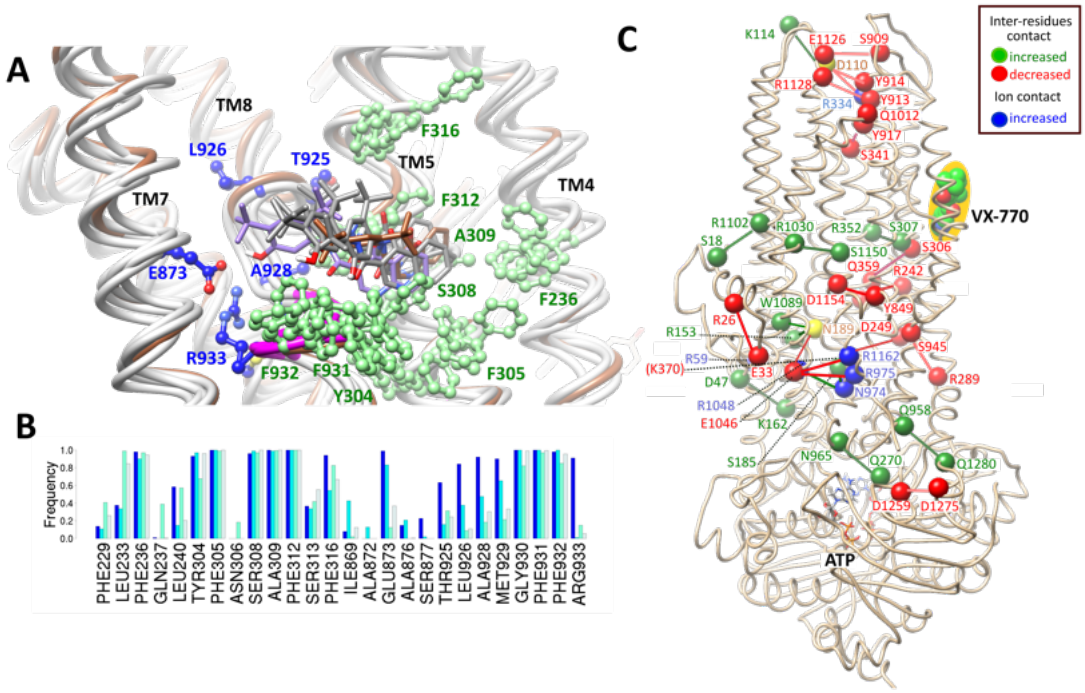

Figure 7: VX-770 binding and effect on the electrostatic interactions. A. View of the VX-770 binding site and the main contacts that the drug establishes with amino acids from TM4, TM5, TM7 and TM8, depicted in atomic details. The 3D structures at the end of the ligand-bound MD simulations were superimposed to the experimental 3D structure of human CFTR, in complex with VX-770 (pdb 6OP2, colored in brown). Conserved contacts relative to the cryo-EM 3D structure are shown in green, while novel contacts (VX1 MD simulation) are depicted in dark blue (VX-770 is shown in purple). The 930-933 segment, which is in helical conformation only in the VX-bound conditions, is colored in magenta. **B.** Barplot displaying the frequency of contacts between CFTR amino acids and VX-770 during the four ligand-bound MD replicates: VX1 (blue), VX2 (cyan), VX3 (aquamarine) and VX4 (azure). Each bar corresponds to a residue that formed a contact with VX-770, and the y-axis indicates the fraction of simulation time the contact was maintained. **C.** View of the CFTR 3D structure (pdb 6O2P), on which are reported amino acids (Cα atoms only) involved in electrostatic interactions and whose contact frequencies (%) differ significantly (≥ 25% for side-chain/side-chain interactions, ≥ 20% for interactions of side chains with ions) between the apo and VX770-bound conditions, as reported in **Table S3**. The pairs involved in side-chain/side-chain interactions are linked with bars. ASP110 and ASN189 (yellow) participate in two different bonds, which are respectively increased (ASP110-LYS114 and ASN189-ARG153/ASN189-TRP1089) and decreased (ASP110-ARG334 and ASN189-ARG1048) in the VX-770-bound conditions, while ARG334 also sees an increase in anion contact. ARG975 and ARG1162 are both involved in interactions decreased (with GLU1046) and increased (with anions) in the presence of VX-770.

Modulation of electrostatic interactions by VX-770

We next compared the prevalence of each electrostatic interaction between the Apo and VX-770–bound conditions to detect potential drug-induced shifts. **Figure S12A** plots the mean contact frequency of each electrostatic interaction in the absence (x-axis) versus presence (y-axis) of VX-770. Most data points lie along the diagonal, indicating that the majority of electrostatic interactions are maintained at comparable frequencies across both conditions. This overall conservation suggests that VX-770 binding does not globally alter CFTR's interaction

network, consistent with its mode of action as a potentiator that enhances channel function without inducing large-scale structural rearrangements.

However, several notable exceptions were identified, reported in **Table S3**, with outliers with contact frequency differences greater than 25% labeled in **Figure S12A** and highlighted in green/red on the 3D structure shown in **Figure 7C.** Bonds with significantly increased frequencies (green in **Figure 7C**) are concentrated into specific areas relative to the membrane plane, at the level of (i) the ECLs ($ASP110_{ECL1}$-$LYS114_{ECL1}$), ii) the VX-770 binding site ($ARG352_{TM6}$–$SER307_{TM5}$), the upper part of the TM10/TM12 portal ($ARG1030_{TM10}$–$SER1150_{TM12}$) and the TMD-lasso interface ($ARG1102_{TM11}$–$SER18_{lasso}$), iii) the ICL:NBD interface. This suggests a local stabilization of the corresponding regions, which supports – in the case of the TM10/TM12 portal - selective anion coordination or permeation through this alternative route. Conversely, several electrostatic interactions were less observed or lost in the VX-770 condition (red in **Figure 7C**). I nterestingly, in the extracellular region, frequency increase of $LYS114_{ECL1}$–$ASP110_{ECL1}$ bond (+51%) coincided with loss of the ECL3 $ARG334_{TM6}$–$ASP110_{ECL1}$ interaction (-39%), potentially facilitating opening of the outer vestibule to support ion permeation. A similar trend was observed with the loss of $SER909_{ECL4}$–$GLU1126_{ECL6}$ (-31%), suggesting a loosening of extracellular contacts in the presence of VX-770. At the TM4/TM6 portal, a striking reduction in the $LYS370_{TM6}$–$ASP249_{TM4}$ (-45%) contact may reflect increased accessibility for anion entry, consistent with the potentiating effect of VX-770. Several weakened interactions were also observed at the level of the intracellular vestibule and bottom part of the TM10/TM12 portal (e.g. $ARG289_{TM5}$–$SER945_{TM8}$), reflecting subtle modulations in these regions, which may be coupled to the correlated reinforcement of other bonds.

Altogether, these observations support a model in which VX-770 enhances CFTR gating by allosterically modulating dynamic interactions across gating-relevant regions.

Changes in anion and lipid contacts upon VX-770 binding

We also examined whether VX-770 binding influences the interaction of CFTR's charged and polar residues with anions and lipids (**Table S3, Figure S12B**).

Only a few residues exhibited a substantial increase (≥20%) in anion contact in the presence of VX-770, notably $ARG59_{lh2}$, $ASN974_{TM9}$, $ARG975_{TM9}$ and $ARG1162_{TM12}$ (dark blue in **Figure 7C**). These three last residues belong to the TM10/TM12 portal, in which other residues also show a more modest increase ($ARG1048_{TM10}$, $SER1045_{TM10}$, SER1049 and $ARG1158_{TM12}$). For most of them, no significant anion interactions were observed under apo conditions. This suggests that VX-770 binding may indirectly enhance the anion attraction at the TM10/TM12 portal, potentially increasing its accessibility or affinity for anions.

A parallel comparison for lipid headgroup contacts (analyzed by lipid type) is shown in **Figure S12C (also see Table S3)**. Most residues exhibited minimal differences, suggesting that CFTR's overall membrane association remains largely unchanged upon VX-770 binding. However, some residues at the protein–lipid interface displayed notable positive shifts. Among them, ARG1128$_{TM10}$, located at the extracellular vestibule, showed marked increase in cholesterol contacts. Contacts with POPS globally decreased in favor of an increase with other lipids, in particular POPE (strong increase of contacts with ARG21$_{lh1}$/ARG1102$_{TM11}$ and ARG899$_{ECL4}$) and POPC (strong increase of contacts with ARG242$_{TM4}$/ASN71$_{elbow1}$/ARG80$_{TM1}$ and ARG25$_{lh1}$). These shifts suggest that VX-770 may subtly remodel lipid engagement at specific sites, possibly influencing signaling across the membrane.

Towards channel opening

The crucial question that currently remains is that of the opening of the channel on its extracellular side, a mechanism that has not yet been revealed by any 3D structure obtained by cryo-EM. An in-depth analysis of MD simulations in the absence and presence of VX-770 shows two exit pathways occurring intermittently, but without these being particularly favored in the presence of the potentiator (**Figures 5B/D and Table S4**). The analysis of water flux and ion occupancy within the membrane slice (centered on the selectivity filter region) did not reveal a statistically significant effect of VX-770 in the conditions of its observed position, as the differences between apo and VX trajectories remained within error bars. The first extracellular exit, surrounded by TM1 and TM6 (TM1-6 exit), in the passage of which PHE337$_{TM6}$ is found, is either non present, small or, for the first replicate in the presence of VX-770 (VX1), larger and conditioned by a PHE337$_{TM6}$ rotamer. The VX1 replicate stood out by allowing a greater number of ions to enter the membrane slab. Notably, this trajectory displayed particularly stable and stronger contacts not only with GLU873$_{TM7}$ and ARG933$_{TM8}$, which together form the anchoring salt bridge of the VX-770 binding pocket, but also with surrounding residues of the unwound TM8 segment, including THR925$_{TM8}$, LEU926$_{TM8}$, ALA928$_{TM8}$, and MET929$_{TM8}$. This suggests that enhanced stabilization of the TM8 region by VX-770 may facilitate ion capture, thereby representing an early premise of channel opening. A similar route was already highlighted by Farkas et al, using metadynamics on the zebrafish CFTR 3D structure [14], as well as by a more recent study having conducted massively repeated simulations starting from chloride permeable conformations [48]. The second exit observed here is displayed between ECL1 and ECL6 (ECL1-6 exit, thus at the center of the 4-helix bundle formed by TM1-TM12 (inner side) and TM2-TM11 (outer side)), which is either closed, of reduced size and conditional (Apo4), or even large in the case of the Apo3 MD simulation. This exit is similar to the one called TM1-TM12 presented in the study of [48] mentioned above. In our Apo3 replica, after 1 μs of MD simulation, the interaction of ARG117$_{ECL1}$ with a lipid led to close this conditional exit in its terminal part, while this closure can

easily be lifted when ARG117$_{ECL1}$ interacts with E1124$_{ECL6}$. Consideration of ECL4 in its entirety (while this one is incomplete in the cryo-EM 3D structures) appears critical for the conformation of the whole set of ECLs and for the opening mechanism, in particular involving the interaction ARG899$_{ECL4}$ with lipids.

Discussion

In this comprehensive study, we have performed microsecond-long, all-atom unbiased molecular dynamics (MD) simulations of the human CFTR 3D structure embedded in a mixed and asymmetric lipid bilayer to investigate how electrostatic interactions involving amino acid side chains — specifically salt bridges and hydrogen bonds — shape the protein's architecture, dynamics and functions. By comparing apo and VX-770–bound states, we provide mechanistic insights into how electrostatic networks (protein-protein, protein-ion and protein-lipid interactions) and transmembrane helix irregularities may contribute to CFTR gating and potentiation. Our findings illustrate several key features that cannot be captured by static cryo-EM 3D structures alone, including the dynamics of bond switching, the influence of the lipid environment, and the coupling between helix deformability and specific stable or transient interactions.

We identified 558 electrostatic interactions between amino acid side chains across CFTR domains, which we classified by frequency and location on the 3D structure. Many highly stable bonds allow specific interactions between TM helices that are particularly strong in the low dielectric environment of the membrane [49], and enable the anchoring of domains in relation to one another—particularly at the level of the elbow, lasso, and ICLs/NBD interfaces. These stable, "architectural" salt-bridges are consistent with the "connecting" principle proposed for immune receptors [49,50] where such interactions constrain conformational flexibility and maintain global fold integrity [51]. Several arginine residues involved in stable SBs, such as ARG347$_{TM6}$ and ARG933$_{TM9}$, establish additional hydrogen bonds with main chain atoms (for ARG347$_{TM6}$ with PHE310$_{TM5}$ and PHE311$_{TM5}$ and for ARG933$_{TM9}$ with CYS866$_{TM7}$ and PHE870$_{TM7}$). This allows adding structural rigidity, a property already observed in other systems [52]. In contrast, dynamic or less stable electrostatic interactions are concentrated in regions where functional transitions related to gating may occur, such as the TM4/6 and TM10/12 portals, and frequently involved in anion coordination. These "functional bonds" (as opposed to the "architectural" term used above) fluctuate during simulations and often involve basic residues that also contact chloride or bicarbonate ions. This mirrors mechanisms described in other transporters and ion channels, where salt-bridge switching has been shown to underlie conformational transitions or channel activation (*e.g.* references [53–56]). It is important to note that several amino acids, notably ASN189

$_{TM3}$, ASN974$_{TM9}$, ASP979$_{TM9}$, ASP984$_{TM9}$ and ARG1158$_{TM12}$ (**Table S5**), have been identified here as central hubs, exhibiting a large number (≥ 5) of electrostatic interactions.

A striking result of our analysis is the tight correlation between electrostatic interactions and transmembrane helix irregularities—regions where α-helical geometry is locally disrupted. These include π-helix bulges, 3_{10}-helix constrictions, or unwound segments, which are increasingly recognized as evolutionarily conserved "weak spots" enabling conformational changes due to a larger plasticity [57]. In CFTR, we show that most residues located in irregularities are directly involved in electrostatic interactions, supporting a model where local electrostatic interactions act on helix flexibility to modulate gating functions. TM irregularities associated with electrostatic interactions cluster into two distinct regions, namely the intracellular vestibule/portals region and the unwound TM8 segment. The inherent flexibility associated with non-stable electrostatic interactions in the intracellular vestibule/portals region are consistent with its role in anion coordination and permeation. Interestingly, this region also includes several gain-of-function variants affecting basic residues (e.g. LYS978$_{TM9}$ [58], ARG1030 $_{TM10}$ and ARG1158$_{TM12}$ [59], supporting the fact that the electrostatic interactions in which they are involved plays a key role in potentiation mechanisms. The central, unwound segment of TM8 contributes to CFTR's structural asymmetry and was proposed to support gating-specific rearrangements [15,60]. Remarkably, this unwound segment has a very stable conformation all along our MD simulations, as it was also observed in previous MD studies [61,62]. This region is flanked by two salt-bridges, which also proved to be particularly stable in our MD simulations: ARG347$_{TM6}$–ASP924$_{TM8}$ and ARG933$_{TM8}$–GLU873$_{TM7}$. Comparison of the experimental 3D structures of ATP-free and ATP-bound CFTR [63], as well of CFTR in the presence of the inhibitor inh-172 (bound at the same level than VX-770 but within the pore [64,65]) indicated that the extracellular portions of TM8 (ending at ASP924$_{TM8}$), TM12 and TM1 are flexible and mobile, representing key actors in the CFTR gating apparatus. ASP924$_{TM8}$ may thus act as a pivot around which conformational transitions occur at the extracellular side, while maintaining a stable base on the unwound segment pillar. Interestingly, we find that the ARG933$_{TM8}$–GLU873 $_{TM7}$ bridge is consistently present (100 % frequency) in both apo and VX-770-bound MD simulations, suggesting a critical role in stabilizing the TM8 unwinding and maintaining the architecture of this region, thereby contributing to the integrity of the VX-770 binding pocket. Moreover, we also highlighted in our MD simulations different positions of the extracellular portions of TM8, coupled with movements of TM12 and TM1, and with the appearance of clear exits towards the extracellular milieu (TM1-6 and ECL1-6 exits, **Figures 5B/D**), suggesting a transition towards an open channel. Notably, in a work that predates the resolution of CFTR cryo-EM structures, the ARG347$_{TM6}$–ASP924$_{TM8}$ interaction was shown to be essential for open-state stabilization [32], along with another salt bridge, ARG352$_{TM6}$-ASP993$_{TM9}$. While the latter is

visible in cryo-EM 3D structures, it appears less stable in our simulations. Instead, ASP993$_{TM9}$ preferentially pairs with ARG303$_{TM5}$, leaving ARG352$_{TM6}$ more available for anion coordination. Intriguingly, ARG352$_{TM6}$ is also located within a helix irregularity (a π-helix segment), reinforcing the notion that such residues act as regulatory switches whose availability and functional role depend on dynamic bond engagement.

Although VX-770 did not globally alter the CFTR salt bridge landscape, it did stabilize specific networks, while it also stabilized the TM8 α-helical structure following its unwound segment (amino acids 930-933). In particular, ARG352$_{TM6}$–SER307$_{TM5}$ and ARG1030$_{TM10}$–SER1150$_{TM12}$ interactions increased in frequency, especially near the TM10/12 portal, a region that also exhibited increased anion and lipid interactions. These changes point to localized tightening and enhanced electrostatic attraction in the drug-bound state, potentially increasing the likelihood of pore opening or ion conduction via this alternative portal. Interestingly, VX-770 also strengthened contacts between the lasso motif and TM11 (e.g. ARG1102$_{TM11}$–SER18$_{lasso}$), indicating a role for peripheral elements near the membrane in stabilizing gating-relevant conformations. Both ARG1102$_{TM11}$ and SER18$_{lasso}$ directly contact VX-445 (Elexacaftor) reported in this region [47], supporting a potential convergence of VX-770 and VX-445 potentiation mechanisms in this region. Finally, increased (albeit modest) contact frequency at the NBD1–NBD2 interface (LYS611$_{NBD1}$-SER1444$_{NBD2}$, +14%) suggests that VX-770 may indirectly enhance ATP-binding domain coupling. This mirrors stabilization mechanisms described in certain ABCA transporters, such as ABCA4 and ABCA7, where additional cytoplasmic regulatory domains (RD1 and RD2) adopt a domain-swapped configuration (each interacting with the opposite NBD) to promote dimerization [66–68]. In CFTR, VX-770 may serve an analogous role, by reinforcing intra- and interdomain communication and priming the channel for gating. Conversely, some contact frequencies decreased in the drug-bound state — particularly some ECLs salt bridges like ARG334$_{TM6/ECL3}$–ASP110$_{ECL1}$ — potentially contributing to opening of the outer vestibule and promoting ion efflux. The likely important role of ECLs in the gating mechanism was already pointed out in the work of Simon and Csanady [24]. In our analysis, their role is all the more obvious here, as the long ECL4 is considered in its entirety. Despite this and although some first insights have been gained on the dynamics of lateral portals and extracellular exits, the studies presented here only lead to observe transient openings of the channel, which undoubtedly requires additional factors to be taken into account. N-glycosylation of ECL4 could be a critical factor, in addition to its role in CFTR folding and trafficking [69].

Compared to ABCC transporters and its closest paralog ABCC4 [19,70], CFTR has evolved through a number of pathways to adopt a regulated channel behavior (reviewed in [10]). Notably, Infield et al. demonstrated that the CFTR chloride channel evolved by utilizing residues that were

already functionally important in the transport of organic anionic substrates in ABCC transporters (i.e. LYS95$_{TM1}$, ARG248$_{TM4}$, ARG303$_{TM5}$, LYS370$_{TM6}$, ARG1030$_{TM10}$, LYS1041$_{TM10}$, ARG1048$_{TM10}$), and repurposing them for the new function of conducting inorganic anions through the channel pore. This is consistent with the overall conservation of pore-lining residues of several TMs [10], with the notable exception of TM6, a highly discriminatory feature of CFTR that may account for neofunctionalization [71,72]. The highly divergent TM6 is directly involved in the formation of a lateral portal (TM4/6 portal) at the level of the intracellular loops, allowing anion to flow from the cytoplasm to the internal vestibule. TM6 also contains two arginine residues (ARG347$_{TM6}$ and ARG352$_{TM6}$), which are involved in electrostatic interactions with surrounding helices (with ASP924$_{TM8}$ and ASP993$_{TM9}$, respectively), although as we have shown here, ARG352$_{TM6}$ is more frequently left free in favor of the interaction of ASP993$_{TM9}$ with ARG303$_{TM5}$. These salt-bridges are included in a key network specific to CFTR at the level of the unwound segment of TM8 (another specific feature of CFTR already discussed above), also including the stable ARG933$_{TM8}$-GLU873$_{TM7}$ salt-bridge. Remarkably, only one of the two partners in each of these electrostatic interactions is conserved in ABCC4 (ARG347$_{TM6}$, ASP993$_{TM9}$ and ARG933$_{TM8}$), while the second ones are VAL, LEU and GLN, respectively (**Table S5**). The emergence of these electrostatic interactions in CFTR has been proposed to stabilize the open conformation of the pore, while we evidence here that ARG352$_{TM6}$ likely plays a direct, key role in the regulation of anion conduction. In line with this observation, it was proposed that the positive charge of ARG352$_{TM6}$ contributes to an electrostatic potential in the channel that forms a barrier to cation permeation [73], while reduced chloride conductance is observed with the rare p.Arg352Gln mutation [74]. Overall, beyond these critical SBs, we show here that CFTR has developed a specific network of electrostatic interactions, involving residues which are only partially conserved in ABCC4 (**Table S5**), suggesting the acquisition of novel functional features from an ancestral network linked to organic anion binding. Thus, it is likely that the larger and more complex network of electrostatic interactions of CFTR contributes, on the one hand, to stabilize the open conformation of the channel and, on the other hand, to regulate its activity. With this specific feature of CFTR clearly highlighted, it is also interesting to note the conservation, between ABCC4 and CFTR, of the extensive interaction networks around ASN189$_{TM3}$ and ASN974$_{TM9}$ at the level of the intracellular vestibule (**Table S5**), highlighting their likely key role in the architecture of a closed intracellular gate.

Beyond interactions linking amino acids together, our study highlights the importance of CFTR's coupling to ions and to its membrane environment, revealing among other amino acids which are involved in multiple types of interaction (**Figure S13**). Limited information is available about this environment and its influence on CFTR function and regulation. A few works have shown that CFTR is located in specialized membrane, detergent-resistant domains at the cell

surface, assembled from clustered lipids - principally cholesterol and sphingomyelin [75–77]. Moreover, a few studies have provided evidence of a direct influence of lipids on the intrinsic CFTR activity (phosphadylserine: [46], cholesterol: [44,45]). Here we showed that specific basic and polar residues engage in frequent contacts with cholesterol and phosphatidylserine (POPS), forming distinct lipid-binding patches. Notably, the lasso domain and elbow regions exhibited high POPS occupancy, consistent with the established role of these CFTR regions in membrane insertion. A TM4–TM5 region, located near the VX-770 binding site, also displayed organized cholesterol and POPS interactions, particularly involving $ARG242_{TM4}$, $LYS246_{TM4}$, and $ARG297_{TM5}$, suggesting a membrane-mediated pathway for allosteric communication between the drug-binding cleft and the transmembrane core. Several of these residues do not participate in salt bridges or ion contacts, reinforcing their specialized role in lipid coupling. Besides direct binding coupled to allosteric communications, lipids can impose mechanical forces that affect the protein function, especially by modification of the membrane fluidity (for a review see [78]). One may also wonder about the role played by the lasso, a segment largely inserted into lipids and interacting strongly with their polar heads, on the properties of the membrane, in particular its curvature.

Overall, this comprehensive mapping of the CFTR interaction network provides valuable insight into the mechanisms of channel activation. Relatively few amino acids of this network are subject to missense mutations (CF-causing (CF) or with varying clinical significance (VCC), **Table S5**). Several of them are strictly conserved in the ABCC4 sequence, suggesting that they play critical role in the ABC architectural template. They include, in the TMDs, amino acids from the ECLs (p.Asp110His/Glu, p.Arg117His/Cys/Leu/Gly/Pro, p.Glu116Lys, p.Arg334Trp/Leu/Gln, p.Ser1118Phe), key amino acids of the TMD central core (p.Glu92Lys, p.Gln98Arg, p.His139Arg, p.Ser341Pro, p.Arg347Pro/His and p.Asp924Asn (both amino acids interacting together), p.Arg352Gln/Trp, p.Asp1152His) and at the level of the inner vestibule/portals (p.Asp192Gly, p.Arg258Gly, p.Ser977Phe, p.Asp979Val, p.His1085Pro, p.Ser1159Phe/Pro). Are also affected residues linking TMD2 to lasso helix 1 (p.Tyr1032Cys, p.Trp1098Arg), belonging to the VX-445 (Elexacaftor)-binding site [47], as well as a set of amino acids linking the lasso and elbow helix of TMD1 (p.Glu56Lys, p.Glu60Lys, p.Arg74Trp), a region that has been shown to be essential for folding and stabilization by the correctors VX-809/VX-661 [34,79]. Several mutations are also found at the ICL:NBD and NBD1:NBD2 interface (**Table S5**). Our study could thus open up interesting avenues for the rational design of pharmacological approaches to correct these mutations and, more generally, to stabilize the open state regardless of the mutation considered.

This work also illustrates the power of MD simulations to uncover structural and dynamic features that are invisible to static experimental techniques. We capture not only the stability of specific electrostatic interactions but also their switching behavior, interactions with lipids and

ions, and their coupling to helix plasticity - all of which are essential for mechanistic understanding. Nonetheless, some limitations remain. Forcefield inaccuracies may affect the fine energetics of anion coordination and conduction. Importantly, the additive force fields used here are not designed to simulate ATP hydrolysis or to accurately capture large-scale conformational changes (such as the transitions toward the inward-facing state starting from the ATP-bound cryo-EM structure), or events such as helix winding and unwinding, which are likely critical for CFTR gating. Moreover, while our simulations show clear openings of the channel, we only observed transient conduction states. Future studies incorporating enhanced sampling methods, longer simulation timescales, or polarizable force fields could help address some of these limitations, as also could the consideration of new parameters that have not yet been taken into account. As a pragmatic, a low-cost alternative to explicit polarization is the use of electronic continuum correction (ECC), including a uniform charge scaling in non-polarizable force fields [80]. This approach can mitigate ion overbinding and improve transport properties when used consistently with an ECC-compatible water model, though care is needed to avoid overscaling artifacts. On the other hand, inclusion of phosphoinositides like PIP2 (phosphatidylinositol-4,5-bisphosphate) in the membrane bilayer, which have been shown to be implicated in CFTR modulation of gating that is highly dependent on the channel phosphorylation state [81], may help complete the picture of membrane-driven modulation. Finally, as pointed before, proper N-linked glycosylation of the extracellular loops may also participate in the modulation of CFTR gating. Glycosylation could thus be necessary to stabilize the open state of CFTR, so explicitly modeling glycan chains in future simulations would be informative.

Materials and methods

System preparation and molecular dynamics simulations

All molecular dynamics (MD) simulations were performed starting from a high-resolution cryo-EM structure of human CFTR in the ATP-bound, phosphorylated (E1371Q) conformation (outward occluded conformation) (PDB ID 6O2P), solved at ~3.3 Å resolution in presence of the potentiator VX-770 (ivacaftor) [15]. Missing extracellular loops (ECLs) were modeled and all titratable residues were assigned their standard protonation states at pH 7.4. The protein was embedded in a heterogeneous and asymmetric phospholipid bilayer composed of POPC (1-palmitoyl-2- oleoylphosphatidylcholine), POPE (1-palmitoyl-2-oleoylphosphatidylethanolamine), CHL1 (cholesterol), DSM (sphingolipid) and POPS (1-palmitoyl-2-oleoylphosphatidylserine) – at an approximate ratio of 3:3:2:1:1 as proposed by [25]. The protein was positioned within the membrane bilayer using the PPM (Positioning of Proteins in Membranes) server [82,83]. The system was assembled using the CHARMM-GUI membrane builder workflow [84,85]. Physiological ionic strength was achieved by adding 150 mM NaCl. In addition, a small and variable amount of

sodium bicarbonate ($NaHCO_3$) was included to represent the presence of bicarbonate anions in the solution, given CFTR's known bicarbonate conductance (**Table S1**).

The system was parameterized with the CHARMM36m force field for the protein, lipids and ions, and TIP3P water molecules were used [86]. The VX-770 parameters were calculated using the CHARMM General Force Field (CGenFF) [87] in CHARMM-GUI ligand modeler module [88]. Energy minimization (5000 steepest descent steps) was first performed to remove bad contacts, followed by a six-stage equilibration protocol. The first three equilibration steps were performed under NVT conditions, followed by the last three steps under NPT conditions, all at a temperature of 310 K. Position restraints on the protein heavy atoms (and VX-770, in the bound cases) and the lipid heads were applied initially and slowly released over the 6 stages (~1.9 ns), allowing the membrane and protein to relax and the solvent to equilibrate. Production runs were then carried out in the NPT ensemble at 310 K, 1 bar with periodic boundary conditions.

Simulations performed with GROMACS (versions 2020.3 and 2023.2) [89] employed Nose–Hoover thermostat and Parrinello–Rahman barostat [90,91] or, alternatively, the V-rescale and C-rescale algorithms [92,93], with LINCS constraints on bonds to hydrogen [94]. One simulation was performed in NAMD2.14 [95] using langevin dynamics [96] and SHAKE constraints on bonds to hydrogen [97]. The use of different thermostat–barostat combinations, as well as Langevin dynamics, allowed us to confirm that our results are consistent across coupling schemes, which differ mainly in numerical stability, relaxation timescales and damping but are equivalent in their ability to sample the NPT ensemble. A 2 fs integration time step was used in all cases, and long-range electrostatic interactions were computed with the Particle Mesh Ewald method [98]. Eight independent MD trajectories were generated in total: four for the apo CFTR (Apo1, Apo2, Apo3, Apo4) and four for the VX-770–bound state (VX1, VX2, VX3, VX4). Simulations were run either for 500 or 1000 ns, yielding an aggregate simulation time of 6 μs for analysis (**Table S1**).

Contacts analysis

Electrostatic contacts involving amino acids, anions, lipid headgroups, and VX-770 were calculated using the VLDM (Voronoi Laguerre Delaunay for Macromolecules) program [99,100]. VLDM relies on a tessellation method—that is, a partition of space into a collection of polyhedra that fill space without overlaps or gaps. Delaunay tessellation and its Laguerre dual were performed using a set of heavy-atom Cartesian coordinates and weights based on the van der Waals radii of the atoms, as defined by the CHARMM36m force field. Two atoms are considered to be in contact if they share a common polygonal face within the tessellation, allowing for a rigorous, geometry-based definition of interatomic interactions. The contact interface between molecular groups is quantified as the sum of the polygonal surface areas shared between their respective atoms.

For the analysis of the contacts, we focused on amino acids typically engaged in electrostatic interactions—namely arginine (ARG), lysine (LYS), glutamic acid (GLU) and aspartic acid (ASP), and we also included histidine (HIS), serine (SER) and threonine (THR), as well as asparagine (ASN), glutamine (GLN), tyrosine (TYR), tryptophane (TRP) and cysteine (CYS). Salt bridges (SBs) and hydrogen bonds (HBs), were defined as side chain-side chain electrostatic interactions between nitrogen or oxygen atoms of these residues. In addition, we also quantified side chain (N/O atoms of ARG, LYS, HIS, SER, THR, ASP, GLU, ASN, GLN, TYR, TRP, CYS) to main chain (backbone N/O atoms) hydrogen bonds, considering only residue pairs separated by more than five amino acids along the sequence. Anion contacts were identified when basic residues (ARG, LYS, HIS) and SER/THR/ASN/GLN/TYR/TRP shared a tessellation face with non-carbon heavy atoms from bicarbonate (HCO_3^-) or with chloride (Cl^-) ions. Lipid interactions were similarly defined as contacts between the same residues and non-carbon heavy atoms from the headgroups of lipid molecules. VX-770 contacts were calculated by considering all heavy atoms of both the ligand and all the protein residues.

For each simulation frame, VLDM generated contact data, which were aggregated over time using in-house R scripts to compute the frequency of each contact, expressed as the percentage of frames in which the contact occurred. These scripts also enabled the combination of contact frequency data across all simulation replicas, the export of the combined data as CSV files, and the generation of comparative bar plots.

The resulting tables were further analyzed using in-house Python scripts. First, contact frequencies were averaged across all simulation replicas. To focus on relevant contacts, only those with a mean frequency equal to or greater than 10% were retained. Next, the distribution of averaged electrostatic interactions across the regions in the CFTR 3D structure was determined (see next subsections), and overlaps between residues forming electrostatic interactions and those involved in anion or lipid contacts, as well as with those involved in alpha-helix irregularities, were calculated. This integrative analysis enabled a detailed annotation of the electrostatic interactions.

CFTR region classification by z-coordinate

To analyze results by protein region, a coordinate-based scheme was applied to assign each residue (and each electrostatic interaction) to a structural/functional domain of CFTR along the Z-axis. The Z-coordinate of each residue's Cα atom involved in an electrostatic interaction was extracted from a CFTR PDB structure and used to determine its regional assignment. Five regions were delineated based on natural breaks in the CFTR structure: (1) NBDs: residues with $Z < 30$ Å; (2) ICLs/NBD interface: residues with $Z \approx 30–53$ Å, covering the ICLs and adjacent regions of the NBDs in contact with the TMDs; (3) Elbow/Lasso/ICLs region: $Z \approx 53–65$ Å, including the elbow helices, lasso motif at the N-terminus, and cytoplasmic ends of

transmembrane helices near the inner leaflet; (4) TM helices/Membrane: residues within the lipid bilayer, with Z ≈ 65–105 Å, corresponding to the membrane-spanning core; and (5) ECLs: residues with Z > 105 Å, located on the extracellular side, including loop segments connecting TM helices. Using this scheme, each electrostatic interaction was assigned to one of the defined CFTR functional regions.

Secondary structure and TM helix irregularity analysis

To probe secondary structure dynamics, we used the DSSP algorithm [101] via *cpptraj* [102] to assign the secondary structure of each residue within CFTR's transmembrane helices (TMs 1–12) throughout the trajectories. For each simulation, we calculated helical occupancy—the fraction of frames in which a residue was assigned as α-helix (as opposed to turn, coil, 3_{10}-helix, etc.). Residues with consistently high occupancy (≈100%) were considered part of stable helical regions, while those with occupancy below 80% (showing variability) were flagged as helix irregularity sites.

Table S2 summarizes these results, listing all ARG, LYS, HIS, ASP, GLU, SER, THR, ASN, GLN, TYR, TRP, CYS residues within TM helices that exhibited <80% helical occupancy in any simulation. For each, the table reports helical occupancy across all simulation replicas (Apo1–4, VX1–4) and indicates whether the residue participated in electrostatic interactions and/or made notable contacts with anions. This integrative analysis allowed us to correlate the helix irregular sites with the different types of interactions.

Data processing and visualization

Trajectory analyses were performed using a combination of VMD Tcl scripts and in-house Python scripts. In the Python workflow, MDAnalysis was used to manage trajectory input/output [103,104]. Additional analyses, such as averaging contact frequencies across replicates and identifying significant differences between conditions, were carried out using NumPy and pandas in Python. To compare apo and VX-770 conditions, the apo trajectories were treated as independent samples, as were the VX-770 trajectories. Mean values were computed, and Δfrequency > 0.3 were considered notable given the sampling length.

Bar plots, scatter plots, and overlap analyses (based on residue list intersections) were generated using Matplotlib, with consistent color schemes applied to represent regions and contact types. Three-dimensional molecular visualizations were created with PyMOL [105] or Chimera [106]. Residue mapping was based on coordinates from the initial cryo-EM structure (PDB ID: 6O2P). PML files were generated to color residues according to their structural region or their involvement in specific types of interactions.

Acknowledgments

This work was performed using HPC resources from GENCI-[CINES] (Grants 2017-A0020707206, 2018-A0040707206, 2019-A0060707206 and 2020-A0080707206) and benefited from the financial support of the French Association Vaincre la Mucoviscidose.

Data and Software availability

MD simulations data (pdb files and trajectories / topology and parameters files / GROMACS entry files), analysis data (contact frequencies, secondary structures) and scripts for analyzing them are provided on Zenodo at https://zenodo.org/records/17646796 . The jupyter-lab notebook (image generation from tsv files) is also provided. The VLDM program and the scripts used to generate contact frequencies must be requested from the program author (Christophe Oguey).

References

(1) Ratjen, F.; Bell, S. C.; Rowe, S. M.; Goss, C. H.; Quittner, A. L.; Bush, A. Cystic Fibrosis. *Nat. Rev. Dis. Primer* **2015**, *1* (1), 15010. https://doi.org/10.1038/nrdp.2015.10.

(2) Thomas, C.; Aller, S. G.; Beis, K.; Carpenter, E. P.; Chang, G.; Chen, L.; Dassa, E.; Dean, M.; Duong Van Hoa, F.; Ekiert, D.; Ford, R.; Gaudet, R.; Gong, X.; Holland, I. B.; Huang, Y.; Kahne, D. K.; Kato, H.; Koronakis, V.; Koth, C. M.; Lee, Y.; Lewinson, O.; Lill, R.; Martinoia, E.; Murakami, S.; Pinkett, H. W.; Poolman, B.; Rosenbaum, D.; Sarkadi, B.; Schmitt, L.; Schneider, E.; Shi, Y.; Shyng, S.; Slotboom, D. J.; Tajkhorshid, E.; Tieleman, D. P.; Ueda, K.; Váradi, A.; Wen, P.; Yan, N.; Zhang, P.; Zheng, H.; Zimmer, J.; Tampé, R. Structural and Functional Diversity Calls for a New Classification of ABC Transporters. *FEBS Lett.* **2020**, *594* (23), 3767–3775. https://doi.org/10.1002/1873-3468.13935.

(3) Alam, A.; Locher, K. P. Structure and Mechanism of Human ABC Transporters. *Annu. Rev. Biophys.* **2023**, *52* (1), 275–300. https://doi.org/10.1146/annurev-biophys-111622-091232.

(4) Thomas, C.; Tampé, R. Structural and Mechanistic Principles of ABC Transporters. *Annu. Rev. Biochem.* **2020**, *89* (1), 605–636. https://doi.org/10.1146/annurev-biochem-011520-105201.

(5) Wang, J.-Q.; Yang, Y.; Cai, C.-Y.; Teng, Q.-X.; Cui, Q.; Lin, J.; Assaraf, Y. G.; Chen, Z.-S. Multidrug Resistance Proteins (MRPs): Structure, Function and the Overcoming of Cancer Multidrug Resistance. *Drug Resist. Updat.* **2021**, *54*, 100743. https://doi.org/10.1016/j.drup.2021.100743.

(6) Russel, F.; Koenderink, J.; Masereeuw, R. Multidrug Resistance Protein 4 (MRP4/ABCC4): A Versatile Efflux Transporter for Drugs and Signalling Molecules. *Trends Pharmacol. Sci.* **2008**, *29* (4), 200–207. https://doi.org/10.1016/j.tips.2008.01.006.

(7) Van Der Sluijs, P.; Hoelen, H.; Schmidt, A.; Braakman, I. The Folding Pathway of ABC Transporter CFTR: Effective and Robust. *J. Mol. Biol.* **2024**, *436* (14), 168591. https://doi.org/10.1016/j.jmb.2024.168591.

(8) Zhang, Z.; Chen, J. Atomic Structure of the Cystic Fibrosis Transmembrane Conductance Regulator. *Cell* **2016**, *167* (6), 1586-1597.e9. https://doi.org/10.1016/j.cell.2016.11.014.

(9) Stolarczyk, E. I.; Reiling, C. J.; Paumi, C. M. Regulation of ABC Transporter Function Via Phosphorylation by Protein Kinases. *Curr. Pharm. Biotechnol.* **2011**, *12* (4), 621–635. https://doi.org/10.2174/138920111795164075.

(10) Infield, D. T.; Strickland, K. M.; Gaggar, A.; McCarty, N. A. The Molecular Evolution of Function in the CFTR Chloride Channel. *J. Gen. Physiol.* **2021**, *153* (12), e202012625. https://doi.org/10.1085/jgp.202012625.
(11) Bai, Y.; Li, M.; Hwang, T.-C. Structural Basis for the Channel Function of a Degraded ABC Transporter, CFTR (ABCC7). *J. Gen. Physiol.* **2011**, *138* (5), 495–507. https://doi.org/10.1085/jgp.201110705.
(12) Hwang, T.-C.; Yeh, J.-T.; Zhang, J.; Yu, Y.-C.; Yeh, H.-I.; Destefano, S. Structural Mechanisms of CFTR Function and Dysfunction. *J. Gen. Physiol.* **2018**, *150* (4), 539–570. https://doi.org/10.1085/jgp.201711946.
(13) Mornon, J.-P.; Hoffmann, B.; Jonic, S.; Lehn, P.; Callebaut, I. Full-Open and Closed CFTR Channels, with Lateral Tunnels from the Cytoplasm and an Alternative Position of the F508 Region, as Revealed by Molecular Dynamics. *Cell. Mol. Life Sci.* **2015**, *72* (7), 1377–1403. https://doi.org/10.1007/s00018-014-1749-2.
(14) Farkas, B.; Tordai, H.; Padányi, R.; Tordai, A.; Gera, J.; Paragi, G.; Hegedűs, T. Discovering the Chloride Pathway in the CFTR Channel. *Cell. Mol. Life Sci.* **2020**, *77* (4), 765–778. https://doi.org/10.1007/s00018-019-03211-4.
(15) Liu, F.; Zhang, Z.; Levit, A.; Levring, J.; Touhara, K. K.; Shoichet, B. K.; Chen, J. Structural Identification of a Hotspot on CFTR for Potentiation. *Science* **2019**, *364* (6446), 1184–1188. https://doi.org/10.1126/science.aaw7611.
(16) Levring, J.; Chen, J. Structural Identification of a Selectivity Filter in CFTR. *Proc. Natl. Acad. Sci.* **2024**, *121* (9), e2316673121. https://doi.org/10.1073/pnas.2316673121.
(17) Cotten, J. F.; Welsh, M. J. Cystic Fibrosis-Associated Mutations at Arginine 347 Alter the Pore Architecture of CFTR. *J. Biol. Chem.* **1999**, *274* (9), 5429–5435. https://doi.org/10.1074/jbc.274.9.5429.
(18) Cui, G.; Zhang, Z.-R.; O'Brien, A. R. W.; Song, B.; McCarty, N. A. Mutations at Arginine 352 Alter the Pore Architecture of CFTR. *J. Membr. Biol.* **2008**, *222* (2), 91–106. https://doi.org/10.1007/s00232-008-9105-9.
(19) King Jordan, I.; Kota, K. C.; Cui, G.; Thompson, C. H.; McCarty, N. A. Evolutionary and Functional Divergence between the Cystic Fibrosis Transmembrane Conductance Regulator and Related ATP-Binding Cassette Transporters. *Proc. Natl. Acad. Sci.* **2008**, *105* (48), 18865–18870. https://doi.org/10.1073/pnas.0806306105.
(20) Zhang, Z.; Liu, F.; Chen, J. Molecular Structure of the ATP-Bound, Phosphorylated Human CFTR. *Proc. Natl. Acad. Sci.* **2018**, *115* (50), 12757–12762. https://doi.org/10.1073/pnas.1815287115.
(21) Billet, A.; Mornon, J.-P.; Jollivet, M.; Lehn, P.; Callebaut, I.; Becq, F. CFTR: Effect of ICL2 and ICL4 Amino Acids in Close Spatial Proximity on the Current Properties of the Channel. *J. Cyst. Fibros.* **2013**, *12* (6), 737–745. https://doi.org/10.1016/j.jcf.2013.02.002.
(22) Wang, W.; Roessler, B. C.; Kirk, K. L. An Electrostatic Interaction at the Tetrahelix Bundle Promotes Phosphorylation-Dependent Cystic Fibrosis Transmembrane Conductance Regulator (CFTR) Channel Opening. *J. Biol. Chem.* **2014**, *289* (44), 30364–30378. https://doi.org/10.1074/jbc.M114.595710.
(23) Cui, G.; Rahman, K. S.; Infield, D. T.; Kuang, C.; Prince, C. Z.; McCarty, N. A. Three Charged Amino Acids in Extracellular Loop 1 Are Involved in Maintaining the Outer Pore Architecture of CFTR. *J. Gen. Physiol.* **2014**, *144* (2), 159–179. https://doi.org/10.1085/jgp.201311122.
(24) Simon, M. A.; Csanády, L. Molecular Pathology of the R117H Cystic Fibrosis Mutation Is Explained by Loss of a Hydrogen Bond. *eLife* **2021**, *10*, e74693. https://doi.org/10.7554/eLife.74693.
(25) Domicevica, L.; Koldsø, H.; Biggin, P. C. Multiscale Molecular Dynamics Simulations of Lipid Interactions with P-Glycoprotein in a Complex Membrane. *J. Mol. Graph. Model.* **2018**, *80*, 147–156. https://doi.org/10.1016/j.jmgm.2017.12.022.
(26) Wong, S. L.; Awatade, N. T.; Astore, M. A.; Allan, K. M.; Carnell, M. J.; Slapetova, I.; Chen, P.; Capraro, A.; Fawcett, L. K.; Whan, R. M.; Griffith, R.; Ooi, C. Y.; Kuyucak, S.; Jaffe, A.; Waters, S. A. Molecular Dynamics and Functional Characterization of I37R-CFTR Lasso

Mutation Provide Insights into Channel Gating Activity. *iScience* **2022**, *25* (1), 103710. https://doi.org/10.1016/j.isci.2021.103710.
(27) Barreto-Ojeda, E.; Corradi, V.; Gu, R.-X.; Tieleman, D. P. Coarse-Grained Molecular Dynamics Simulations Reveal Lipid Access Pathways in P-Glycoprotein. *J. Gen. Physiol.* **2018**, *150* (3), 417–429. https://doi.org/10.1085/jgp.201711907.
(28) Corradi, V.; Mendez-Villuendas, E.; Ingólfsson, H. I.; Gu, R.-X.; Siuda, I.; Melo, M. N.; Moussatova, A.; DeGagné, L. J.; Sejdiu, B. I.; Singh, G.; Wassenaar, T. A.; Delgado Magnero, K.; Marrink, S. J.; Tieleman, D. P. Lipid–Protein Interactions Are Unique Fingerprints for Membrane Proteins. *ACS Cent. Sci.* **2018**, *4* (6), 709–717. https://doi.org/10.1021/acscentsci.8b00143.
(29) Khodadadi, E.; Khodadadi, E.; Chaturvedi, P.; Moradi, M. Comprehensive Insights into the Cholesterol-Mediated Modulation of Membrane Function Through Molecular Dynamics Simulations. *Membranes* **2025**, *15* (6), 173. https://doi.org/10.3390/membranes15060173.
(30) Pornillos, O.; Chang, G. Inverted Repeat Domains in Membrane Proteins. *FEBS Lett.* **2006**, *580* (2), 358–362. https://doi.org/10.1016/j.febslet.2005.12.054.
(31) Negoda, A.; Hogan, M. S.; Cowley, E. A.; Linsdell, P. Contribution of the Eighth Transmembrane Segment to the Function of the CFTR Chloride Channel Pore. *Cell. Mol. Life Sci.* **2019**, *76* (12), 2411–2423. https://doi.org/10.1007/s00018-019-03043-2.
(32) Cui, G.; Freeman, C. S.; Knotts, T.; Prince, C. Z.; Kuang, C.; McCarty, N. A. Two Salt Bridges Differentially Contribute to the Maintenance of Cystic Fibrosis Transmembrane Conductance Regulator (CFTR) Channel Function. *J. Biol. Chem.* **2013**, *288* (28), 20758–20767. https://doi.org/10.1074/jbc.M113.476226.
(33) Fiedorczuk, K.; Chen, J. Mechanism of CFTR Correction by Type I Folding Correctors. *Cell* **2022**, *185* (1), 158-168.e11. https://doi.org/10.1016/j.cell.2021.12.009.
(34) Baatallah, N.; Elbahnsi, A.; Mornon, J.-P.; Chevalier, B.; Pranke, I.; Servel, N.; Zelli, R.; Décout, J.-L.; Edelman, A.; Sermet-Gaudelus, I.; Callebaut, I.; Hinzpeter, A. Pharmacological Chaperones Improve Intra-Domain Stability and Inter-Domain Assembly via Distinct Binding Sites to Rescue Misfolded CFTR. *Cell. Mol. Life Sci.* **2021**, *78* (23), 7813–7829. https://doi.org/10.1007/s00018-021-03994-5.
(35) Pesce, E.; Tomati, V.; Capurro, V.; Lena, M.; Pastorino, C.; Astore, M.; Kuyucak, S.; Chevalier, B.; Sondo, E.; Cresta, F.; Dighero, A.; Terlizzi, V.; Fevola, C.; Costa, S.; Lucanto, M. C.; Daccò, V.; Claut, L.; Ficili, F.; Fabrizzi, B.; Bocciardi, R.; Zara, F.; Castellani, C.; Galietta, L. J. V.; Waters, S. A.; Hinzpeter, A.; Pedemonte, N. *In Silico* , *in Vitro and Ex Vivo* Characterization of Cystic Fibrosis Transmembrane Conductance Regulator Pathogenic Variants Localized in the Fourth Intracellular Loop and Their Rescue by Modulators. *Br. J. Pharmacol.* **2025**, bph.70176. https://doi.org/10.1111/bph.70176.
(36) Basso, C.; Vergani, P.; Nairn, A. C.; Gadsby, D. C. Prolonged Nonhydrolytic Interaction of Nucleotide with CFTR's NH2-Terminal Nucleotide Binding Domain and Its Role in Channel Gating. *J. Gen. Physiol.* **2003**, *122* (3), 333–348. https://doi.org/10.1085/jgp.200308798.
(37) Stockner, T.; Gradisch, R.; Schmitt, L. The Role of the Degenerate Nucleotide Binding Site in Type I ABC Exporters. *FEBS Lett.* **2020**, *594* (23), 3815–3838. https://doi.org/10.1002/1873-3468.13997.
(38) Sorum, B.; Töröcsik, B.; Csanády, L. Asymmetry of Movements in CFTR's Two ATP Sites during Pore Opening Serves Their Distinct Functions. *eLife* **2017**, *6*, e29013. https://doi.org/10.7554/eLife.29013.
(39) Zhou, Z.; Wang, X.; Liu, H.-Y.; Zou, X.; Li, M.; Hwang, T.-C. The Two ATP Binding Sites of Cystic Fibrosis Transmembrane Conductance Regulator (CFTR) Play Distinct Roles in Gating Kinetics and Energetics. *J. Gen. Physiol.* **2006**, *128* (4), 413–422. https://doi.org/10.1085/jgp.200609622.
(40) Hohl, M.; Hürlimann, L. M.; Böhm, S.; Schöppe, J.; Grütter, M. G.; Bordignon, E.; Seeger, M. A. Structural Basis for Allosteric Cross-Talk between the Asymmetric Nucleotide

Binding Sites of a Heterodimeric ABC Exporter. *Proc. Natl. Acad. Sci.* **2014**, *111* (30), 11025–11030. https://doi.org/10.1073/pnas.1400485111.
(41) El Hiani, Y.; Negoda, A.; Linsdell, P. Cytoplasmic Pathway Followed by Chloride Ions to Enter the CFTR Channel Pore. *Cell. Mol. Life Sci. CMLS* **2016**, *73* (9), 1917–1925. https://doi.org/10.1007/s00018-015-2113-x.
(42) El Hiani, Y.; Linsdell, P. Functional Architecture of the Cytoplasmic Entrance to the Cystic Fibrosis Transmembrane Conductance Regulator Chloride Channel Pore. *J. Biol. Chem.* **2015**, *290* (25), 15855–15865. https://doi.org/10.1074/jbc.M115.656181.
(43) Linsdell, P. Architecture and Functional Properties of the CFTR Channel Pore. *Cell. Mol. Life Sci. CMLS* **2017**, *74* (1), 67–83. https://doi.org/10.1007/s00018-016-2389-5.
(44) Chin, S.; Ramjeesingh, M.; Hung, M.; Ereño-Oreba, J.; Cui, H.; Laselva, O.; Julien, J.-P.; Bear, C. E. Cholesterol Interaction Directly Enhances Intrinsic Activity of the Cystic Fibrosis Transmembrane Conductance Regulator (CFTR). *Cells* **2019**, *8* (8), 804. https://doi.org/10.3390/cells8080804.
(45) Cui, G.; Cottrill, K. A.; Strickland, K. M.; Mashburn, S. A.; Koval, M.; McCarty, N. A. Alteration of Membrane Cholesterol Content Plays a Key Role in Regulation of Cystic Fibrosis Transmembrane Conductance Regulator Channel Activity. *Front. Physiol.* **2021**, *12*, 652513. https://doi.org/10.3389/fphys.2021.652513.
(46) Hildebrandt, E.; Khazanov, N.; Kappes, J. C.; Dai, Q.; Senderowitz, H.; Urbatsch, I. L. Specific Stabilization of CFTR by Phosphatidylserine. *Biochim. Biophys. Acta BBA - Biomembr.* **2017**, *1859* (2), 289–293. https://doi.org/10.1016/j.bbamem.2016.11.013.
(47) Fiedorczuk, K.; Chen, J. Molecular Structures Reveal Synergistic Rescue of Δ508 CFTR by Trikafta Modulators. *Science* **2022**, *378* (6617), 284–290. https://doi.org/10.1126/science.ade2216.
(48) Zeng, Z.-W.; Ing, C. E.; Pomès, R. Structure and Cl- Conductance Properties of the Open State of Human CFTR. February 21, 2025. https://doi.org/10.7554/eLife.105722.1.
(49) Walther, T. H.; Ulrich, A. S. Transmembrane Helix Assembly and the Role of Salt Bridges. *Curr. Opin. Struct. Biol.* **2014**, *27*, 63–68. https://doi.org/10.1016/j.sbi.2014.05.003.
(50) Call, M. E.; Wucherpfennig, K. W.; Chou, J. J. The Structural Basis for Intramembrane Assembly of an Activating Immunoreceptor Complex. *Nat. Immunol.* **2010**, *11* (11), 1023–1029. https://doi.org/10.1038/ni.1943.
(51) Kumar, S.; Nussinov, R. Close-Range Electrostatic Interactions in Proteins. *ChemBioChem* **2002**, *3* (7), 604. https://doi.org/10.1002/1439-7633(20020703)3:7%253C604::AID-CBIC604%253E3.0.CO;2-X.
(52) Borders, C. L.; Broadwater, J. A.; Bekeny, P. A.; Salmon, J. E.; Lee, A. S.; Eldridge, A. M.; Pett, V. B. A Structural Role for Arginine in Proteins: Multiple Hydrogen Bonds to Backbone Carbonyl Oxygens. *Protein Sci.* **1994**, *3* (4), 541–548. https://doi.org/10.1002/pro.5560030402.
(53) DeCaen, P. G.; Yarov-Yarovoy, V.; Zhao, Y.; Scheuer, T.; Catterall, W. A. Disulfide Locking a Sodium Channel Voltage Sensor Reveals Ion Pair Formation during Activation. *Proc. Natl. Acad. Sci.* **2008**, *105* (39), 15142–15147. https://doi.org/10.1073/pnas.0806486105.
(54) Dibb, K. M.; Rose, T.; Makary, S. Y.; Claydon, T. W.; Enkvetchakul, D.; Leach, R.; Nichols, C. G.; Boyett, M. R. Molecular Basis of Ion Selectivity, Block, and Rectification of the Inward Rectifier Kir3.1/Kir3.4 K+ Channel. *J. Biol. Chem.* **2003**, *278* (49), 49537–49548. https://doi.org/10.1074/jbc.M307723200.
(55) Nakajo, K.; Kubo, Y. Second Coiled□coil Domain of KCNQ Channel Controls Current Expression and Subfamily Specific Heteromultimerization by Salt Bridge Networks. *J. Physiol.* **2008**, *586* (12), 2827–2840. https://doi.org/10.1113/jphysiol.2007.148601.
(56) Sackin, H.; Nanazashvili, M.; Li, H.; Palmer, L. G.; Walters, D. E. An Intersubunit Salt Bridge near the Selectivity Filter Stabilizes the Active State of Kir1.1. *Biophys. J.* **2009**, *97* (4), 1058–1066. https://doi.org/10.1016/j.bpj.2009.05.056.
(57) Bibbe, J. M.; Vriend, G. Motions around Conserved Helical Weak Spots Facilitate GPCR Activation. *Proteins Struct. Funct. Bioinforma.* **2021**, *89* (11), 1577–1586. https://doi.org/10.1002/prot.26179.

(58) Wang, W.; Wu, J.; Bernard, K.; Li, G.; Wang, G.; Bevensee, M. O.; Kirk, K. L. ATP-Independent CFTR Channel Gating and Allosteric Modulation by Phosphorylation. *Proc. Natl. Acad. Sci.* **2010**, *107* (8), 3888–3893. https://doi.org/10.1073/pnas.0913001107.
(59) Castanier, S.; Elbahnsi, A.; Chevalier, B.; Baatallah, N.; Pranke, I.; Berri, L.; Edelman, A.; Sermet-Gaudelus, I.; Mornon, J.-P.; Callebaut, I.; Hinzpeter, A. Novel Gain-of-Function Mutants Identify a Critical Region within CFTR Membrane-Spanning Domain 2 Controlling cAMP-Dependent and ATP-Independent Channel Activation. *Cell. Mol. Life Sci.* **2024**, *81* (1), 426. https://doi.org/10.1007/s00018-024-05431-9.
(60) Liu, F.; Zhang, Z.; Csanády, L.; Gadsby, D. C.; Chen, J. Molecular Structure of the Human CFTR Ion Channel. *Cell* **2017**, *169* (1), 85-95.e8. https://doi.org/10.1016/j.cell.2017.02.024.
(61) Corradi, V.; Gu, R.-X.; Vergani, P.; Tieleman, D. P. Structure of Transmembrane Helix 8 and Possible Membrane Defects in CFTR. *Biophys. J.* **2018**, *114* (8), 1751–1754. https://doi.org/10.1016/j.bpj.2018.03.003.
(62) Zeng, Z. W.; Linsdell, P.; Pomès, R. Molecular Dynamics Study of Cl− Permeation through Cystic Fibrosis Transmembrane Conductance Regulator (CFTR). *Cell. Mol. Life Sci.* **2023**, *80* (2), 51. https://doi.org/10.1007/s00018-022-04621-7.
(63) Zhang, Z.; Liu, F.; Chen, J. Conformational Changes of CFTR upon Phosphorylation and ATP Binding. *Cell* **2017**, *170* (3), 483-491.e8. https://doi.org/10.1016/j.cell.2017.06.041.
(64) Gao, X.; Yeh, H.-I.; Yang, Z.; Fan, C.; Jiang, F.; Howard, R. J.; Lindahl, E.; Kappes, J. C.; Hwang, T.-C. Allosteric Inhibition of CFTR Gating by CFTRinh-172 Binding in the Pore. *Nat. Commun.* **2024**, *15* (1), 6668. https://doi.org/10.1038/s41467-024-50641-1.
(65) Young, P. G.; Levring, J.; Fiedorczuk, K.; Blanchard, S. C.; Chen, J. Structural Basis for CFTR Inhibition by CFTR $_{inh}$ -172. *Proc. Natl. Acad. Sci.* **2024**, *121* (10), e2316675121. https://doi.org/10.1073/pnas.2316675121.
(66) Liu, F.; Lee, J.; Chen, J. Molecular Structures of the Eukaryotic Retinal Importer ABCA4. *eLife* **2021**, *10*, e63524. https://doi.org/10.7554/eLife.63524.
(67) Xie, T.; Zhang, Z.; Fang, Q.; Du, B.; Gong, X. Structural Basis of Substrate Recognition and Translocation by Human ABCA4. *Nat. Commun.* **2021**, *12* (1), 3853. https://doi.org/10.1038/s41467-021-24194-6.
(68) Le, L. T. M.; Thompson, J. R.; Dehghani□Ghahnaviyeh, S.; Pant, S.; Dang, P. X.; French, J. B.; Kanikeyo, T.; Tajkhorshid, E.; Alam, A. CRYO□EM Structures of Human ABCA7 Provide Insights into Its Phospholipid Translocation Mechanisms. *EMBO J.* **2023**, *42* (3), e111065. https://doi.org/10.15252/embj.2022111065.
(69) Glozman, R.; Okiyoneda, T.; Mulvihill, C. M.; Rini, J. M.; Barriere, H.; Lukacs, G. L. N-Glycans Are Direct Determinants of CFTR Folding and Stability in Secretory and Endocytic Membrane Traffic. *J. Cell Biol.* **2009**, *184* (6), 847–862. https://doi.org/10.1083/jcb.200808124.
(70) Cui, G.; Hong, J.; Chung-Davidson, Y.-W.; Infield, D.; Xu, X.; Li, J.; Simhaev, L.; Khazanov, N.; Stauffer, B.; Imhoff, B.; Cottrill, K.; Blalock, J. E.; Li, W.; Senderowitz, H.; Sorscher, E.; McCarty, N. A.; Gaggar, A. An Ancient CFTR Ortholog Informs Molecular Evolution in ABC Transporters. *Dev. Cell* **2019**, *51* (4), 421-430.e3. https://doi.org/10.1016/j.devcel.2019.09.017.
(71) Kogan, I. CFTR Directly Mediates Nucleotide-Regulated Glutathione Flux. *EMBO J.* **2003**, *22* (9), 1981–1989. https://doi.org/10.1093/emboj/cdg194.
(72) McCarty, N. A.; Zhang, Z.-R. Identification of a Region of Strong Discrimination in the Pore of CFTR. *Am. J. Physiol.-Lung Cell. Mol. Physiol.* **2001**, *281* (4), L852–L867. https://doi.org/10.1152/ajplung.2001.281.4.L852.
(73) Guinamard, R.; Akabas, M. H. Arg352 Is a Major Determinant of Charge Selectivity in the Cystic Fibrosis Transmembrane Conductance Regulator Chloride Channel. *Biochemistry* **1999**, *38* (17), 5528–5537. https://doi.org/10.1021/bi990155n.
(74) Wong, S. L.; Awatade, N. T.; Astore, M. A.; Allan, K. M.; Carnell, M. J.; Slapetova, I.; Chen, P.-C.; Setiadi, J.; Pandzic, E.; Fawcett, L. K.; Widger, J. R.; Whan, R. M.; Griffith, R.; Ooi, C. Y.; Kuyucak, S.; Jaffe, A.; Waters, S. A. Molecular Dynamics and Theratyping in Airway

and Gut Organoids Reveal R352Q-CFTR Conductance Defect. *Am. J. Respir. Cell Mol. Biol.* **2022**, *67* (1), 99–111. https://doi.org/10.1165/rcmb.2021-0337OC.
(75) Abu-Arish, A.; Pandzic, E.; Goepp, J.; Matthes, E.; Hanrahan, J. W.; Wiseman, P. W. Cholesterol Modulates CFTR Confinement in the Plasma Membrane of Primary Epithelial Cells. *Biophys. J.* **2015**, *109* (1), 85–94. https://doi.org/10.1016/j.bpj.2015.04.042.
(76) Dudez, T.; Borot, F.; Huang, S.; Kwak, B. R.; Bacchetta, M.; Ollero, M.; Stanton, B. A.; Chanson, M. CFTR in a Lipid Raft-TNFR1 Complex Modulates Gap Junctional Intercellular Communication and IL-8 Secretion. *Biochim. Biophys. Acta BBA - Mol. Cell Res.* **2008**, *1783* (5), 779–788. https://doi.org/10.1016/j.bbamcr.2008.01.007.
(77) Wang, D.; Wang, W.; Duan, Y.; Sun, Y.; Wang, Y.; Huang, P. Functional Coupling of Gs and CFTR Is Independent of Their Association with Lipid Rafts in Epithelial Cells. *Pflüg. Arch. - Eur. J. Physiol.* **2008**, *456* (5), 929–938. https://doi.org/10.1007/s00424-008-0460-2.
(78) Cottrill, K. A.; Farinha, C. M.; McCarty, N. A. The Bidirectional Relationship between CFTR and Lipids. *Commun. Biol.* **2020**, *3* (1), 179. https://doi.org/10.1038/s42003-020-0909-1.
(79) Kleizen, B.; Van Willigen, M.; Mijnders, M.; Peters, F.; Grudniewska, M.; Hillenaar, T.; Thomas, A.; Kooijman, L.; Peters, K. W.; Frizzell, R.; Van Der Sluijs, P.; Braakman, I. Co-Translational Folding of the First Transmembrane Domain of ABC-Transporter CFTR Is Supported by Assembly with the First Cytosolic Domain. *J. Mol. Biol.* **2021**, *433* (13), 166955. https://doi.org/10.1016/j.jmb.2021.166955.
(80) Fan, S.; Mason, P. E.; Chamorro, V. C.; Shanks, B. L.; Martinez-Seara, H.; Jungwirth, P. Charge Scaling Force Field for Biologically Relevant Ions Utilizing a Global Optimization Method. *J. Chem. Theory Comput.* **2025**, acs.jctc.5c00873. https://doi.org/10.1021/acs.jctc.5c00873.
(81) Vynichaki, I. M.; Csanady, L.; Logothetis, D. E. Regulation of CFTR by the Membrane Phospholipid PIP2. *Biophys. J.* **2024**, *123* (3), 401a. https://doi.org/10.1016/j.bpj.2023.11.2458.
(82) Lomize, A. L.; Todd, S. C.; Pogozheva, I. D. Spatial Arrangement of Proteins in Planar and Curved Membranes by PPM 3.0. *Protein Sci.* **2022**, *31* (1), 209–220. https://doi.org/10.1002/pro.4219.
(83) Lomize, M. A.; Pogozheva, I. D.; Joo, H.; Mosberg, H. I.; Lomize, A. L. OPM Database and PPM Web Server: Resources for Positioning of Proteins in Membranes. *Nucleic Acids Res.* **2012**, *40* (D1), D370–D376. https://doi.org/10.1093/nar/gkr703.
(84) Jo, S.; Kim, T.; Iyer, V. G.; Im, W. CHARMM-GUI: A Web-Based Graphical User Interface for CHARMM. *J. Comput. Chem.* **2008**, *29* (11), 1859–1865. https://doi.org/10.1002/jcc.20945.
(85) Lee, J.; Cheng, X.; Swails, J. M.; Yeom, M. S.; Eastman, P. K.; Lemkul, J. A.; Wei, S.; Buckner, J.; Jeong, J. C.; Qi, Y.; Jo, S.; Pande, V. S.; Case, D. A.; Brooks, C. L.; MacKerell, A. D.; Klauda, J. B.; Im, W. CHARMM-GUI Input Generator for NAMD, GROMACS, AMBER, OpenMM, and CHARMM/OpenMM Simulations Using the CHARMM36 Additive Force Field. *J. Chem. Theory Comput.* **2016**, *12* (1), 405–413. https://doi.org/10.1021/acs.jctc.5b00935.
(86) Huang, J.; MacKerell, A. D. CHARMM36 All-Atom Additive Protein Force Field: Validation Based on Comparison to NMR Data. *J. Comput. Chem.* **2013**, *34* (25), 2135–2145. https://doi.org/10.1002/jcc.23354.
(87) Vanommeslaeghe, K.; Hatcher, E.; Acharya, C.; Kundu, S.; Zhong, S.; Shim, J.; Darian, E.; Guvench, O.; Lopes, P.; Vorobyov, I.; Mackerell, A. D. CHARMM General Force Field: A Force Field for Drug□like Molecules Compatible with the CHARMM All□atom Additive Biological Force Fields. *J. Comput. Chem.* **2010**, *31* (4), 671–690. https://doi.org/10.1002/jcc.21367.
(88) Kim, S.; Lee, J.; Jo, S.; Brooks, C. L.; Lee, H. S.; Im, W. CHARMM-GUI Ligand Reader and Modeler for CHARMM Force Field Generation of Small Molecules: CHARMM-GUI Ligand Reader and Modeler for CHARMM Force Field Generation of Small Molecules. *J. Comput. Chem.* **2017**, *38* (21), 1879–1886. https://doi.org/10.1002/jcc.24829.

(89) Abraham, M. J.; Murtola, T.; Schulz, R.; Páll, S.; Smith, J. C.; Hess, B.; Lindahl, E. GROMACS: High Performance Molecular Simulations through Multi-Level Parallelism from Laptops to Supercomputers. *SoftwareX* **2015**, *1–2*, 19–25. https://doi.org/10.1016/j.softx.2015.06.001.
(90) Nosé, S. A Unified Formulation of the Constant Temperature Molecular Dynamics Methods. *J. Chem. Phys.* **1984**, *81* (1), 511–519. https://doi.org/10.1063/1.447334.
(91) Parrinello, M.; Rahman, A. Polymorphic Transitions in Single Crystals: A New Molecular Dynamics Method. *J. Appl. Phys.* **1981**, *52* (12), 7182–7190. https://doi.org/10.1063/1.328693.
(92) Bussi, G.; Donadio, D.; Parrinello, M. Canonical Sampling through Velocity Rescaling. *J. Chem. Phys.* **2007**, *126* (1), 014101. https://doi.org/10.1063/1.2408420.
(93) Bernetti, M.; Bussi, G. Pressure Control Using Stochastic Cell Rescaling. *J. Chem. Phys.* **2020**, *153* (11), 114107. https://doi.org/10.1063/5.0020514.
(94) Hess, B.; Bekker, H.; Berendsen, H. J. C.; Fraaije, J. G. E. M. LINCS: A Linear Constraint Solver for Molecular Simulations. *J. Comput. Chem.* **1997**, *18* (12), 1463–1472. https://doi.org/10.1002/(SICI)1096-987X(199709)18:12%253C1463::AID-JCC4%253E3.0.CO;2-H.
(95) Phillips, J. C.; Braun, R.; Wang, W.; Gumbart, J.; Tajkhorshid, E.; Villa, E.; Chipot, C.; Skeel, R. D.; Kalé, L.; Schulten, K. Scalable Molecular Dynamics with NAMD. *J. Comput. Chem.* **2005**, *26* (16), 1781–1802. https://doi.org/10.1002/jcc.20289.
(96) Quigley, D.; Probert, M. I. J. Langevin Dynamics in Constant Pressure Extended Systems. *J. Chem. Phys.* **2004**, *120* (24), 11432–11441. https://doi.org/10.1063/1.1755657.
(97) Ryckaert, J.-P.; Ciccotti, G.; Berendsen, H. J. C. Numerical Integration of the Cartesian Equations of Motion of a System with Constraints: Molecular Dynamics of n-Alkanes. *J. Comput. Phys.* **1977**, *23* (3), 327–341. https://doi.org/10.1016/0021-9991(77)90098-5.
(98) Darden, T.; York, D.; Pedersen, L. Particle Mesh Ewald: An $N \cdot \log(N)$ Method for Ewald Sums in Large Systems. *J. Chem. Phys.* **1993**, *98* (12), 10089–10092. https://doi.org/10.1063/1.464397.
(99) Esque, J.; Oguey, C.; De Brevern, A. G. A Novel Evaluation of Residue and Protein Volumes by Means of Laguerre Tessellation. *J. Chem. Inf. Model.* **2010**, *50* (5), 947–960. https://doi.org/10.1021/ci9004892.
(100) Elbahnsi, A.; Retureau, R.; Baaden, M.; Hartmann, B.; Oguey, C. Holding the Nucleosome Together: A Quantitative Description of the DNA–Histone Interface in Solution. *J. Chem. Theory Comput.* **2018**, *14* (2), 1045–1058. https://doi.org/10.1021/acs.jctc.7b00936.
(101) Kabsch, W.; Sander, C. Dictionary of Protein Secondary Structure: Pattern Recognition of Hydrogen-Bonded and Geometrical Features. *Biopolymers* **1983**, *22* (12), 2577–2637. https://doi.org/10.1002/bip.360221211.
(102) Roe, D. R.; Cheatham, T. E. PTRAJ and CPPTRAJ: Software for Processing and Analysis of Molecular Dynamics Trajectory Data. *J. Chem. Theory Comput.* **2013**, *9* (7), 3084–3095. https://doi.org/10.1021/ct400341p.
(103) Gowers, R.; Linke, M.; Barnoud, J.; Reddy, T.; Melo, M.; Seyler, S.; Domański, J.; Dotson, D.; Buchoux, S.; Kenney, I.; Beckstein, O. MDAnalysis: A Python Package for the Rapid Analysis of Molecular Dynamics Simulations; Austin, Texas, 2016; pp 98–105. https://doi.org/10.25080/Majora-629e541a-00e.
(104) Michaud□Agrawal, N.; Denning, E. J.; Woolf, T. B.; Beckstein, O. MDAnalysis: A Toolkit for the Analysis of Molecular Dynamics Simulations. *J. Comput. Chem.* **2011**, *32* (10), 2319–2327. https://doi.org/10.1002/jcc.21787.
(105) Schrödinger, LLC. The PyMOL Molecular Graphics System, Version 1.8, 2015.
(106) Pettersen, E. F.; Goddard, T. D.; Huang, C. C.; Couch, G. S.; Greenblatt, D. M.; Meng, E. C.; Ferrin, T. E. UCSF Chimera—A Visualization System for Exploratory Research and Analysis. *J. Comput. Chem.* **2004**, *25* (13), 1605–1612. https://doi.org/10.1002/jcc.20084.